ARTICLES
PUBLISHED ONLINE: 11 NOVEMBER 2012 | DOI: 10.1038/NMAT3477
nature materials

Resonant light trapping in ultrathin films for water splitting

Hen Dotan[1], Ofer Kfir[2], Elad Sharlin[1], Oshri Blank[1], Moran Gross[1], Irina Dumchin[1], Guy Ankonina[3] and Avner Rothschild[1]*

Semiconductor photoelectrodes for solar hydrogen production by water photoelectrolysis must employ stable, non-toxic, abundant and inexpensive visible-light absorbers. Iron oxide (α-Fe_2O_3) is one of few materials meeting these requirements, but its poor transport properties present challenges for efficient charge-carrier generation, separation, collection and injection. Here we show that these challenges can be addressed by means of resonant light trapping in ultrathin films designed as optical cavities. Interference between forward- and backward-propagating waves enhances the light absorption in quarter-wave or, in some cases, deeper subwavelength films, amplifying the intensity close to the surface wherein photogenerated minority charge carriers (holes) can reach the surface and oxidize water before recombination takes place. Combining this effect with photon retrapping schemes, such as using V-shaped cells, provides efficient light harvesting in ultrathin films of high internal quantum efficiency, overcoming the trade-off between light absorption and charge collection. A water photo-oxidation current density of 4 mA cm^{-2} was achieved using a V-shaped cell comprising ~26-nm-thick Ti-doped α-Fe_2O_3 films on back-reflector substrates coated with silver–gold alloy.

The efficient conversion of solar energy to hydrogen by means of water photoelectrolysis is a long-standing challenge with promise for solar energy conversion and storage in the form of synthetic fuels (so-called solar fuels)[1,2]. Important advances in studying water photoelectrolysis by semiconductor photoelectrodes[3] have been achieved in the past four decades, since the seminal report[4] on photoinduced water splitting using TiO_2 photoanodes. Despite these advances and intensive research and development efforts worldwide no photoelectrochemical system for solar hydrogen production has met the required performance benchmarks for efficiency, durability and cost. Numerous photoelectrodes were examined, but most of them were ruled out owing to poor stability or low efficiency[5,6]. α-Fe_2O_3 (haematite) is one of few materials with a favourable combination of stability in aqueous solutions, visible-light absorption, non-toxicity, abundance and low cost[7–9]. With an energy bandgap of 2.1 eV, α-Fe_2O_3 photoanodes can theoretically reach water photo-oxidation current densities as high as 12.6 mA cm^{-2} under air mass 1.5 global (AM1.5G) solar irradiation conditions[10], potentially enabling a maximum solar to hydrogen conversion efficiency of 15.5% to be reached in an ideal tandem cell configuration[11]. However, because of the low internal quantum efficiency (IQE), only a quarter of the theoretical limit has been achieved by the best α-Fe_2O_3 photoanode reported so far[12].

The low IQE of α-Fe_2O_3 photoanodes has been attributed to the slow water oxidation kinetics[13] and short diffusion length of the photogenerated minority charge carriers (holes)[14] resulting in significant loss due to electron–hole recombination. Extensive efforts have been directed towards enhancing the water oxidation kinetics using catalysts[7,9,12], and reducing bulk recombination by developing nanostructured architectures that decouple the charge transport and optical path lengths[7–9,15]. Nanostructuring thick layers has been the main route to balance the trade-off between light absorption and collection of photogenerated holes[8,9,15]. This trade-off limits the solar energy conversion efficiency of semiconductors with poor transport properties wherein the minority charge-carrier collection length is smaller than the light penetration depth[16]. Despite these efforts, state-of-the-art nanostructured α-Fe_2O_3 photoanodes still exhibit excessive bulk recombination that consumes three quarters, or more, of the photogenerated charge carriers. On the other hand, the injection yield of holes that have reached the surface exceeds 90% under sufficiently high anodic potentials[17]. Recent studies on thick layers[18,19] as well as ultrathin films[20] confirm that the efficiency of α-Fe_2O_3 photoanodes is mainly limited by the collection of photogenerated holes at the surface. Thus, reducing bulk recombination is the key to improving the IQE of α-Fe_2O_3 photoanodes—an important step towards efficient, sustainable, durable and potentially inexpensive solar hydrogen production.

Whereas the conventional approach for balancing photogeneration and collection of minority charge carriers at the surface of α-Fe_2O_3 photoanodes centres around nanostructured porous thick layers ($\geq$0.5 μm) of high surface area, here we show a radically different approach in which compact flat ultrathin films are designed as light trapping structures. Such films can be easily produced using thin-film deposition methods, and they do not have a high surface area that enhances surface recombination and may lower the surface photovoltage—the driving force for photoelectrochemical processes on semiconductor photoelectrodes[21]. Instead of decoupling the optical and charge transport path lengths we exploit the wave-nature of light propagation in subwavelength structures to tailor the light intensity distribution inside the film, amplifying the intensity close to the electrode/electrolyte interface. This enables maximization of the absorption in regions where the

[1]Department of Materials Science and Engineering, Technion—Israel Institute of Technology, Haifa 32000, Israel, [2]Physics Department, Technion—Israel Institute of Technology, Haifa 32000, Israel, [3]Photovoltaics Laboratory, Technion—Israel Institute of Technology, Haifa 32000, Israel.
*e-mail: avnerrot@technion.ac.il.

photogenerated minority charge carriers can reach the surface and minimization of the wasted absorption in regions where they are lost to recombination.

Ultrathin film α-Fe_2O_3 photoanodes

The rationale for using ultrathin (<50 nm) film α-Fe_2O_3 photoanodes stems from their high IQE compared with their thick-layer counterparts[22]. This is demonstrated in Supplementary Fig. S1, which shows that the charge separation and collection yield of photogenerated holes at the surface of Ti-doped α-Fe_2O_3 thin films (Supplementary Fig. S2) increases with decreasing film thickness, reaching 58±6% for the thinnest film (16±5 nm). This exceeds the collection yield found in state-of-the-art nanostructured Si-doped α-Fe_2O_3 thick layers[17] by a factor of three, approximately, demonstrating the potential advantage of ultrathin films of high crystalline quality (see Supplementary Figs S4–S8). The salient problem is that their optical density is too small. The thinnest film, that is the one with the highest collection yield, is nearly translucent (see Supplementary Fig. S2-C). Thus, effective utilization of ultrathin α-Fe_2O_3 films requires special means to enhance the probability of light–matter interaction in subwavelength structures. The standard approach for trapping light in thin film solar cells works only for films much thicker than a half wavelength[23]. This is too thick for α-Fe_2O_3 because of the small collection length of the photogenerated holes in this material[9,13,14]. To address this challenge we employ a resonant light trapping strategy that surpasses the classical limits of statistical ray optics[24], enabling efficient photon harvesting well below the minimum film thickness required for the standard approach.

Resonant light trapping in ultrathin films

Our strategy employs optical cavities comprising ultrathin absorbing films on reflective substrates serving as current collectors and back reflectors that give rise to interference between the forward- and backward-propagating waves, as illustrated schematically in Fig. 1. This enhances the absorption by increasing the photon lifetime in the film, reaching maximum absorption in the cavity resonance modes. For normal incidence on an ideal cavity the first resonance mode occurs in quarter-wave films, that is, when the film thickness (d) is a quarter of the wavelength (λ) of the light inside the film. We note that $\lambda = \lambda_0 n_2^{-1}$, where λ_0 is the wavelength in vacuum and n_2 is the refractive index of the film. The quarter-wave condition takes into account the π phase shifts on reflection from the surface of the film ($x = 0$) and from the film/substrate interface ($x = d$), and another π phase shift on traversing the film forth and back. Consequently, the first-order reflection is in anti-phase with the higher-order reflections, as shown in Fig. 1, thereby suppressing the intensity of the back-reflected light. Moreover, the light intensity increases near the surface owing to constructive interference between the forward- and backward-propagating waves. For other conditions such as oblique light or optical cavities employing metallized substrates with complex refractive indices the optimal film thickness is smaller than a quarter-wave, providing another degree of freedom for optimization.

The quarter-wave resonance condition is well defined for monochromatic light, but our goal is to harvest as many photons as possible from the incident sunlight in a broad spectral range between the absorption edge of the absorber ($\lambda_0^{max} = 590$ nm for α-Fe_2O_3) and the fall-off of the sunlight spectrum ($\lambda_0^{min} = 300$ nm). Therefore, we should find the optimal film thickness for trapping sunlight in this spectral range. Moreover, owing to the strong dependence of the collection efficiency of photogenerated minority charge carriers on the distance from the surface[25] we must take into account not only how many photons are absorbed but also where they are absorbed. The photocurrent density can then be calculated by integrating the product of the photogeneration distribution, which scales with the squared optical electric field strength[26], and

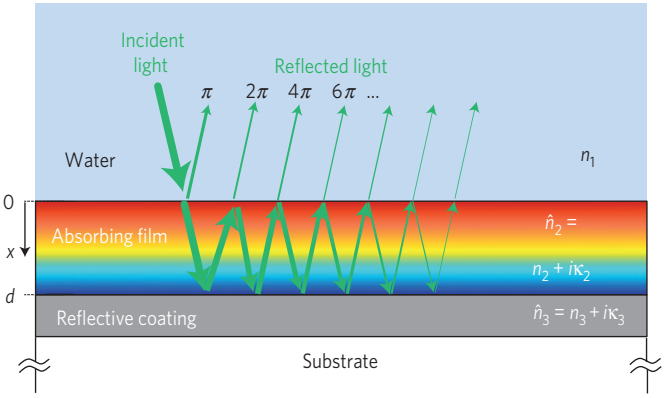

Figure 1 | Resonant light trapping in quarter-wave films. Schematic illustration of the light propagation in a quarter-wave ($d = \lambda/4$, for normal incidence) absorbing film on a back-reflector substrate. The different colours represent the light intensity distribution across the film (red, high; blue, low).

the IQE distribution across the film over the entire film thickness and over the solar irradiance spectrum.

To calculate the light intensity distribution inside the film we take the plane-wave solution of Maxwell's electromagnetic wave equation and tailor it to fit the boundary conditions of our system with incident solar radiation, at AM1.5G conditions, striking the optical stack illustrated in Fig. 1. From these solutions we obtain analytical expressions (see Supplementary Equations S1–S3) for the spectral photon flux profiles (the number of photons of wavelength λ_0 reaching a distance x from the surface per unit time, unit area and unit wavelength) $I_{\lambda_0}(\lambda_0, x)$ for normal incidence on α-Fe_2O_3 films on ideally reflective, transparent or partially reflective metallized substrates with complex refractive indices $\hat{n}_3 = n_3 + i\kappa_3$, where n_3 and κ_3 are the refractive and attenuation indices, respectively. The metallized substrates give rise to complex reflection coefficients at the film/substrate interface[27], $\hat{r}_{23} = (\hat{n}_2 - \hat{n}_3)(\hat{n}_2 + \hat{n}_3)^{-1}$. By integrating $I_{\lambda_0}(\lambda_0, x)$ we obtain the photon flux profiles, $I(x) = \int_{\lambda_0^{min}}^{\lambda_0^{max}} I_{\lambda_0}(\lambda_0, x)\, d\lambda_0$, as a function of depth (x) inside the film.

Photon flux profiles predicted for Ti-doped α-Fe_2O_3 films on ideally reflective ($\hat{r}_{23} = -1$), transparent ($\hat{r}_{23} = 0$) and metallized substrates coated with silver or platinum are shown in Fig. 2. Further profiles for films on aluminium- or gold-coated substrates are presented in Supplementary Fig. S26. The optical constants of the Ti-doped α-Fe_2O_3 films were measured by spectroscopic ellipsometry (see Supplementary Fig. S11) and the constants for the metallized substrates were taken from the ellipsometer database.

The predicted photon flux profiles for films on reflective substrates exhibit a periodic dependence on the film thickness. The first resonance mode of the ideal cavity is predicted to occur at a film thickness of 43 nm, reaching the maximal intensity at the surface. Partially reflective metallized substrates give rise to smaller photon fluxes, due to absorption in the metal coating, and the resonance modes are shifted to smaller film thicknesses due to phase shifts larger than π at the film/substrate interface (see Supplementary Fig. S25). The optical loss due to absorption in the metal coating is low for silver and aluminium, but quite high for platinum and gold. The first resonance mode is predicted to occur at a film thickness of 20, 20, 24 or 30 nm for silver, gold, platinum or aluminium coatings, respectively. Thus, the selection of the reflective coating material influences the optimal film thickness. All in all, considerably larger photon fluxes are predicted in films, of the optimal thickness, on reflective substrates compared with their counterparts on transparent substrates wherein the photons have only one pass through the film and their flux

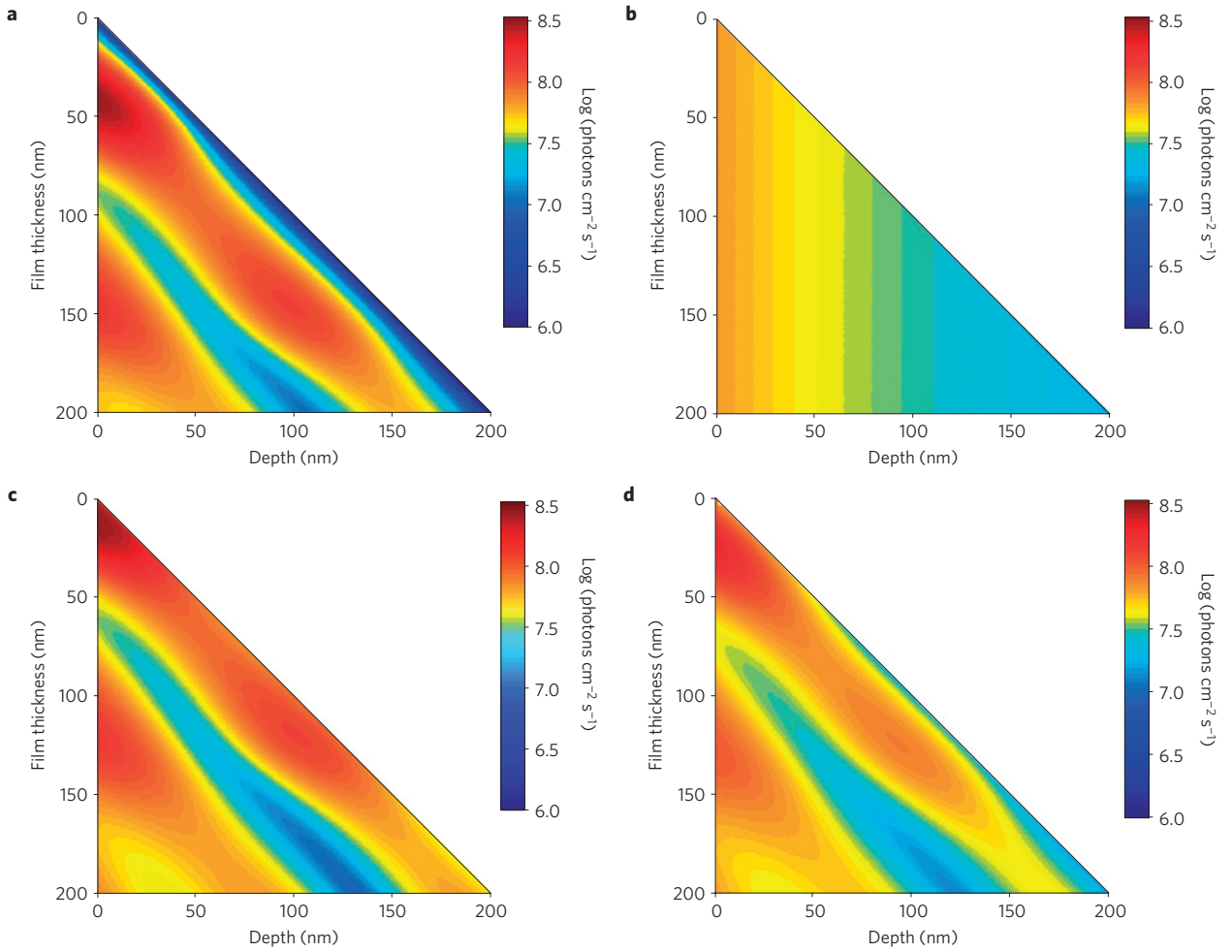

Figure 2 | Light intensity maps. a–d, Predicted photon flux profiles as a function of film thickness and depth from the surface into the film for Ti-doped α-Fe_2O_3 films on ideally reflective (**a**), transparent (**b**) and metallized substrates coated with silver (**c**) or platinum (**d**).

decreases exponentially with x according to Lambert's law with no dependence on the film thickness.

Figure 2 shows that in the first resonance mode high photon fluxes are concentrated close to the surface. This is critical for efficient collection of the photogenerated minority charge carriers, enabling them to reach the surface and drive the water splitting reaction before bulk recombination takes place. Furthermore, the photon flux close to the film/substrate interface is suppressed in films on ideally reflective substrates because of the π phase shift on reflection from an ideal reflector[27]. This is expected to reduce the loss due to backward injection of minority charge carriers to the substrate, which has been identified as a major source of loss in ultrathin α-Fe_2O_3 photoanodes[28].

To verify our model calculations we deposited Ti-doped α-Fe_2O_3 films of different thicknesses between 8 and 155 nm on platinized and, for comparison, fluorinated tin oxide (FTO)-coated glass substrates (see Supplementary Fig. S2). The absorptance spectra, $a(\lambda_0)$, of the specimens were obtained from reflection and transmission measurements (Supplementary Fig. S12). The absorbed photon flux was calculated using the formula[29] $I_{abs} = \int_{\lambda_0^{min}}^{\lambda_0^{max}} I_{\lambda_0}^{Sun}(\lambda_0) a(\lambda_0)\, d\lambda_0$, where $I_{\lambda_0}^{Sun}$ is the solar irradiance spectrum at AM1.5G conditions. The results are shown in Fig. 3 in terms of I_{abs} and the photogenerated current density, $J_{pg} = qI_{abs}$, where q is the elementary charge. The black squares show the absorption in the platinized specimens. The model calculations, shown by the dashed line black curve, nicely fit the experimental results. We note that the absorptance obtained by these measurements includes contributions from both the α-Fe_2O_3 film and the platinized substrate, and we cannot extract directly the net absorption in the α-Fe_2O_3 film. Instead, we show (full line black curve) the predicted absorption in the α-Fe_2O_3 films, obtained by integrating the product of the photon flux profiles in Fig. 2d and the absorption coefficient of the films (Supplementary Fig. S11) over the entire film thickness. Similar calculations for films on ideally reflective ($R = 1$, red curve), transparent ($R = 0$, blue curve) and metallized substrates coated with silver (green curve), aluminium (grey curve) or gold (orange curve) are also shown in Fig. 3. For the translucent FTO-coated specimens we obtain the net absorptance in the Ti-doped α-Fe_2O_3 films from transmission and reflection measurements of coated and uncoated specimens (see Supplementary Fig. S14). These results are shown by the blue circles in Fig. 3.

The absorption in α-Fe_2O_3 films on platinized substrates is predicted to reach the first maximum at a film thickness of 36 nm with a photogenerated current density of 5.1 mA cm^{-2}, that is 40% of the ultimate limit for α-Fe_2O_3 (ref. 10). For comparison, the same film would absorb approximately half the photons (2.8 mA cm^{-2}) if it were on a transparent substrate. Calculations for films on ideally reflective substrates (red curve) show that a 47-nm-thick film would reach a photogenerated current density of 8.9 mA cm^{-2}, that is 71% of the theoretical limit. This demonstrates the effectiveness of our light trapping strategy, as the same film on a transparent substrate yields only 3.4 mA cm^{-2}. Thus, the photon harvesting yield can be nearly tripled by replacing the ubiquitous transparent substrates with suitable back reflectors. Similar calculations for films on silver,

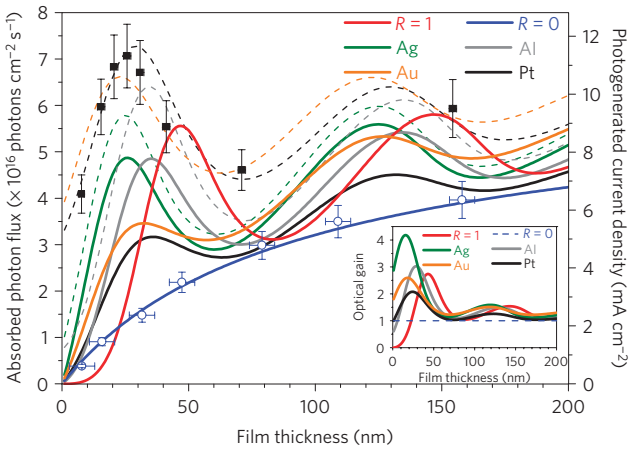

Figure 3 | Sunlight absorption in α-Fe_2O_3 films on back-reflector substrates versus their counterparts on transparent substrates. Absorbed photon flux and the corresponding photogenerated current density as a function of film thickness for specimens comprising Ti-doped α-Fe_2O_3 films on platinized (black squares) or FTO-coated substrates (blue circles). The error bars represent the range of (estimated) systematic errors in the measurements. The dashed curves show the predicted absorption in the entire specimen, comprising contributions from both film and substrate; the solid line curves show the predicted net absorption in the α-Fe_2O_3 films. The inset shows the predicted optical gain, that is, the amount of photons absorbed in α-Fe_2O_3 films on different substrates divided by the absorption in films of the same thickness on FTO-coated substrates.

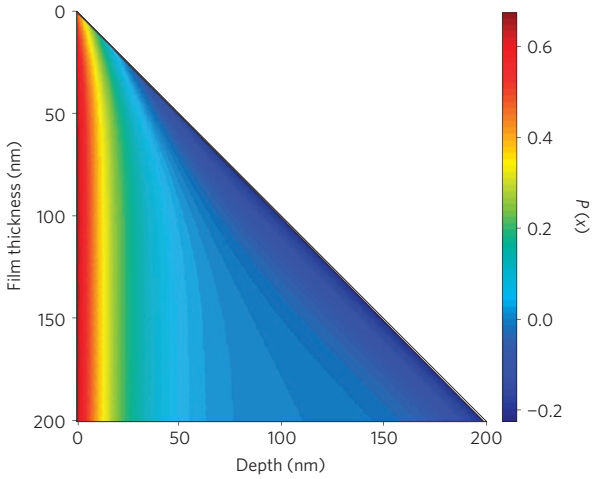

Figure 4 | Internal quantum efficiency map. The predicted IQE distribution inside the film as a function of film thickness and depth for α-Fe_2O_3 films with $\Phi = 0.75$, $\vec{P}_F = \overleftarrow{P}_B = 0.9$ and $L = 20$ nm.

aluminium- and gold-coated substrates are predicted to yield high optical gains (see Fig. 3, inset), with a maximum gain of 4.2 for a 16-nm-thick film on a silver-coated substrate (green curve). It is noteworthy that the rest of the photons that are not absorbed in the α-Fe_2O_3 film are not necessarily lost. The back-reflected photons that escape can be collected using photon retrapping schemes such as using V-shaped cells[30], thereby further boosting the absorption.

From light trapping to water photo-oxidation

The photocurrent density, J_{photo}, is a product of the photogeneration rate per unit time and unit volume at distance x from the surface, $g(x)$, and the IQE distribution function, $P(x)$, integrated over the entire film thickness: $J_{photo}(d) = q\int_0^d g(x)P(x)dx$. The photogeneration rate is a product of the spectral photon flux distribution inside the film, $I_{\lambda_0}(\lambda_0,x)$, and the absorption coefficient of the absorber, $\alpha(\lambda_0)$, integrated over the wavelength range between the absorption edge and the fall-off of the sunlight spectrum[16]: $g(x) = \int_{\lambda_0^{min}}^{\lambda_0^{max}} I_{\lambda_0}(\lambda_0,x)\alpha(\lambda_0)d\lambda_0$. $P(x)$ is the probability for the photogenerated minority charge carriers to separate from the majority carriers, reach the surface and drive the water splitting reaction. Only those carriers that reach the front surface of the film and are forward injected to the electrolyte contribute to the water splitting process, whereas those reaching the backside of the film and being backward injected to the substrate reduce the photocurrent. Backward injection to the substrate may occur by interfacial recombination with charge carriers of the opposite charge arriving from the substrate (that is, the back electrode). We designate by Φ the probability for charge separation and transport in the forward direction, that is, minority charge carriers going towards the surface. The collection probability of minority charge carriers generated at a distance x from the surface scales exponentially with $-x/L$, where L is their collection length[25]. Designating by $\vec{P}_F$ the probability for forward injection to the electrolyte, that is, the probability for minority charge carriers that have reached the surface to drive the desired electrochemical reaction, the fraction of photogenerated minority charge carriers that end up with a positive contribution to the photocurrent is $\vec{P}_F \Phi e^{-x/L}$. Likewise, the fraction of their counterparts ending up with a negative contribution due to backward injection to the substrate is $\overleftarrow{P}_B(1-\Phi)e^{-(d-x)/L}$, where $\overleftarrow{P}_B$ is the probability for backward injection. All in all, $P(x) = \vec{P}_F \Phi e^{-x/L} - \overleftarrow{P}_B(1-\Phi)e^{-(d-x)/L}$. We note that this expression can be derived from the constituent equations of solar cells[31].

$\vec{P}_F, \overleftarrow{P}_B, L$ and Φ depend on the doping level, preparation and operation conditions of the photoelectrode. Figure 4 shows $P(x)$ as a function of d and x for $\Phi = 0.75$, $\vec{P}_F = \overleftarrow{P}_B = 0.9$ and $L = 20$ nm. These values were found to fit quite well the photocurrent densities obtained with our Ti-doped α-Fe_2O_3 films on platinized substrates, and they are within range of the expected values[13,17,32]. $P(x)$ reaches more than 60% close to the surface but it decays exponentially to near zero values deeper than ~20 nm from the surface, reaching negative values close to the interface with the substrate.

Taking the product of $g(x)$, obtained using the calculated photon flux profiles in Fig. 2 and the measured absorption coefficient of our films (Supplementary Fig. S11), and $P(x)$ from Fig. 4 we obtain the predicted photocurrent density per unit volume profiles, $dJ_{photo}/dx = qg(x)P(x)$, for films on ideally reflective, transparent or metallized substrates, as shown in Fig. 5. These profiles show that mainly the front region down to ~20 nm from the surface contributes to the photocurrent. The rest of the film is inactive, for the most part, owing to bulk recombination, whereas the backside of the film has a negative contribution due to backward injection to the substrate. The advantage of our optical cavity design is clearly demonstrated by the hotspots of high photocurrent density close to the surface of films whose thickness is close to the optimal thickness for the first resonance mode. The highest photocurrent densities are predicted for the ideal cavity, which is also effective in reducing the backward injection to the substrate by suppressing the light intensity close to the film/substrate interface (see Fig. 2a). Films on partially reflective metallized substrates also exhibit hotspots of high photocurrent densities, but the hotspots become weaker in going from highly reflective metals such as silver to poorly reflective ones such as platinum. We also note that the calculations suggest that the metallized substrates do not reduce the backward-injection loss as effectively as their ideally reflective counterparts.

The photocurrent density per unit area, J_{photo}, is calculated by integrating the photocurrent density per unit volume over the entire film thickness. Figure 6a shows the predicted photocurrent density as a function of film thickness for α-Fe_2O_3 films on different substrates, assuming ideal forward-injection conditions

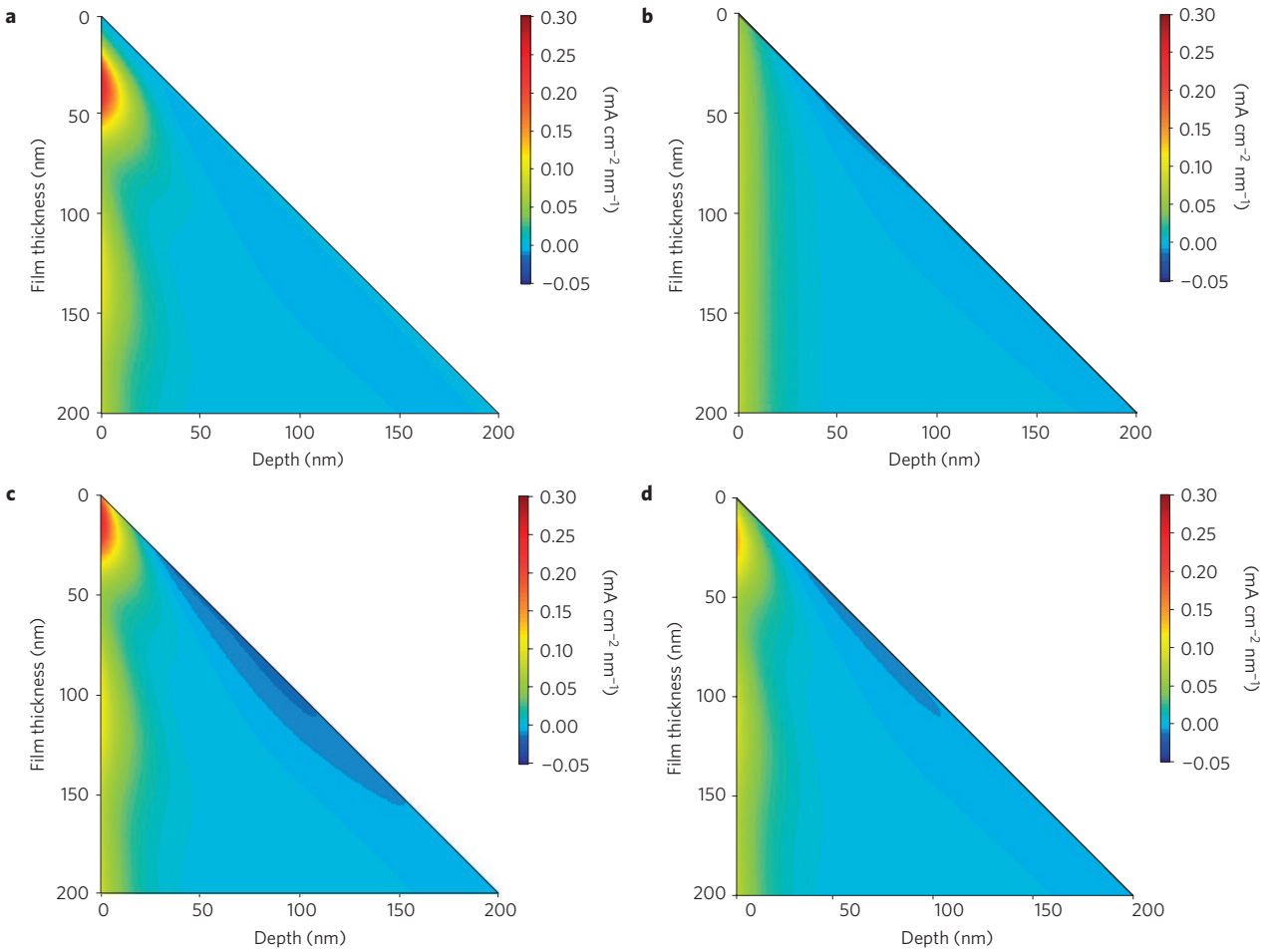

Figure 5 | Photocurrent distribution maps. a–d, Predicted photocurrent density distribution maps as a function of film thickness and depth for α-Fe_2O_3 films on ideally reflective (**a**), transparent (**b**) and metallized substrates coated with silver (**c**) or platinum (**d**). Further profiles for aluminium- and gold-coated substrates are presented in Supplementary Fig. S27.

(that is, $\Phi = 1$ and $\vec{P}_F = 1$). Such conditions may be realized using sufficiently high potentials[17] and selective transport layers to block the backward injection to the substrate[33]. Films on reflective substrates are predicted to yield maximum photocurrents close to the first resonance modes of the respective optical cavities. The maxima are quite narrow and therefore the film thickness must be precisely tuned to achieve the optimal performance, as an offset of just a few nanometres significantly decreases the photocurrent. A maximum of 4.8 mA cm^{-2} is predicted for a 43-nm-thick film on an ideally reflective substrate (red curve). This value exceeds the record obtained with the best α-Fe_2O_3 photoanode reported so far[12], demonstrating the potential advantage of our approach. Photocurrent densities of 4.6, 4.3, 3.1 and 2.9 mA cm^{-2} are predicted for 22-, 31-, 24- and 29-nm-thick α-Fe_2O_3 films on silver-, aluminium-, gold- and platinum-coated substrates, respectively. The predicted photocurrent gain with respect to films of the same thickness on transparent substrates is shown in the inset of Fig. 6a. Optical cavities comprising ultrathin α-Fe_2O_3 films are predicted to exhibit considerable gains reaching 3.6, 2.8, 2.3 and 2.0 for 14-, 28-, 18- and 24-nm-thick films on silver-, aluminium-, gold- or platinum-coated substrates, respectively, whereas the gain for films on ideally reflective substrates reaches 2.9 for a 42-nm-thick film.

To verify our model calculations the photocurrent density of Ti-doped α-Fe_2O_3 films on platinized or, for comparison, FTO-coated substrates was measured in a 1 M NaOH solution under 100 mW cm^{-2} white-light illumination. Figure 6b shows the photocurrent density, measured at an applied potential of 1.4 V against the reversible hydrogen electrode (V_{RHE}), plotted as a function of the film thickness. Further results are shown in Supplementary Figs S15–S17. The photocurrent density reached a maximum of 1.39 ± 0.03 mA cm^{-2} for a 26 ± 2-nm-thick Ti-doped α-Fe_2O_3 film on a platinized substrate, 2.6 times higher than the photocurrent density obtained with a film of about the same thickness (32 ± 8 nm) on an FTO-coated substrate. Moreover, this ultrathin film outperformed any of its counterparts on FTO-coated transparent substrates, including much thicker films. These results clearly demonstrate the advantage of our light trapping scheme, even though these proof-of-concept tests were carried out with structures far from the optimal design because of the high optical loss due to absorption in the platinum coating as well as other losses as described in the following.

The experimental results in Fig. 6b were fitted with model calculations assuming $L = 20 \pm 2$ nm, consistent with other reports[13,32], and taking $\vec{P}_F \times \Phi$ and $\overleftarrow{P}_B \times (1 - \Phi)$ as fitting parameters. All the other parameters were obtained from optical measurements of the specimens (Supplementary Fig. S11). An excellent agreement was obtained with $\vec{P}_F \times \Phi = 0.70 \pm 0.05$ and $\overleftarrow{P}_B \times (1 - \Phi) = 0.25 \pm 0.05$, validating our model calculations. The fitting results are consistent with $\vec{P}_F = 0.95 \pm 0.05$, close to the injection efficiency of our films as measured by the method described in ref. 17, $\overleftarrow{P}_B = 1^{0}_{\pm 0.3}$, and $\Phi = 0.74 \pm 0.07$. Thus, a significant fraction of the potentially achievable photocurrent predicted for these structures is lost for backward injection to the

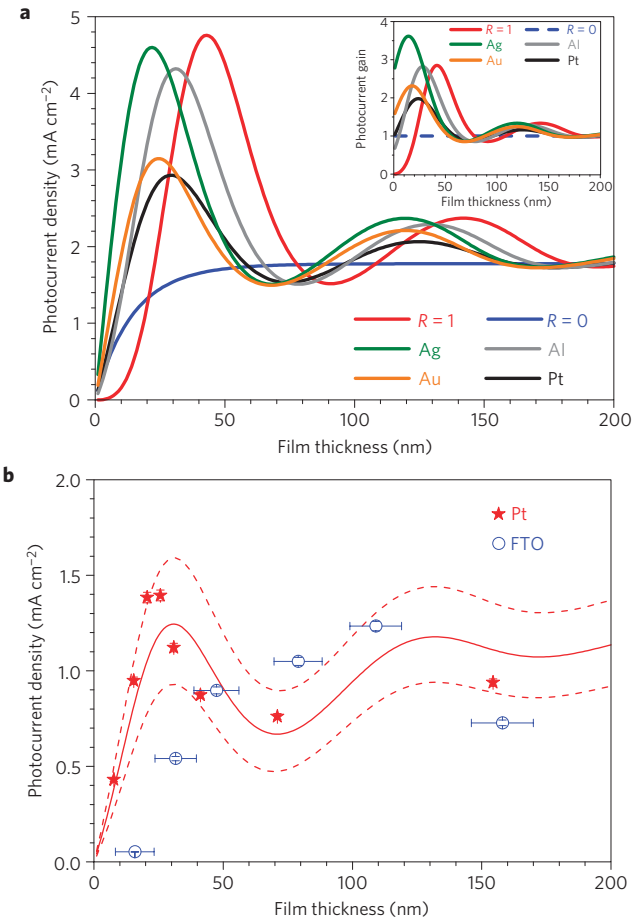

Figure 6 | Photocurrent as a function of film thickness. a, Predicted photocurrent density as a function of film thickness for α-Fe_2O_3 films on different substrates under ideal forward-injection conditions. **b**, Photocurrent density, measured at 1.4 V_{RHE} in 100 mW cm^{-2} white-light illumination, as a function of film thickness for Ti-doped α-Fe_2O_3 films on platinized (red stars) or FTO-coated substrates (blue circles). The error bars represent the range of (estimated) systematic errors in the measurements. The red curves show model calculations for films on platinized substrates taking $L = 20 \pm 2$ nm, $\vec{P}_F \times \Phi = 0.70 \pm 0.05$ and $\overleftarrow{P}_B \times (1 - \Phi) = 0.25 \pm 0.05$.

substrate. This loss highlights the importance of separating the photogenerated holes from the electrons by imposing asymmetric charge transport conditions and blocking the backward injection of holes to the substrate, which is especially critical for ultrathin films wherein a sizeable portion of the photogeneration occurs at the backside of the film[28,33].

Ultrathin α-Fe_2O_3 films on silver-based back reflectors

To improve the results of our light trapping structures we replaced the lossy platinum reflective coatings by silver-based back reflectors and reduced the backward-injection loss by adding selective electron transport layers between the Ti-doped α-Fe_2O_3 films and the substrates. The transition from platinum to silver required developing means to stabilize the back reflectors against tarnishing and thermal etching[34] during the high-temperature deposition of the α-Fe_2O_3 films, as well as against corrosion[35] during the water splitting tests. The best-performing photoanodes were obtained using ~1.2-μm-thick layers of silver–gold alloy with 90 at.% silver and 10 at.% gold, sandwiched between ultrathin TiN diffusion barrier layers and protected from thermal etching by ultrathin SnO_2 over layers (see Supplementary Fig. S6-B). The SnO_2 intermediate

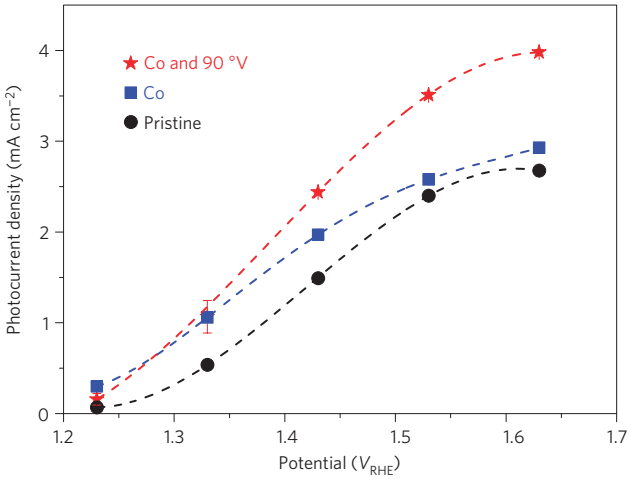

Figure 7 | Water photo-oxidation current densities obtained with ultrathin film α-Fe_2O_3 photoanodes on silver-based back reflectors. Steady-state water photo-oxidation current densities obtained using ultrathin (~26 nm) Ti-doped α-Fe_2O_3 films on silver–gold back reflectors, measured in a 1 M NaOH aqueous solution under exposure to 100 mW cm^{-2} white-light illumination at potentials ranging from 1.23 to 1.63 V_{RHE}. The results for a pristine photoanode with no catalyst are shown as black circles; for a cobalt-treated photoanode as blue squares; and for two cobalt-treated photoanodes placed facing each other in a 90° V-shaped cell as red stars.

layers also served as selective electron transport layers owing to the large valence-band offset[36] between SnO_2 and α-Fe_2O_3 that blocks the injection of holes from the α-Fe_2O_3 films to the substrates. These structures were highly reflective (see Supplementary Fig. S3), remaining so through the entire fabrication process (as can be seen by the interference colours in Supplementary Fig. S2-D), and stable against corrosion during the water splitting tests.

With these structures we obtained water photo-oxidation current densities as high as 2.90 ± 0.01 mA cm^{-2} (at 1.63 V_{RHE}, see Supplementary Fig. S22) for a Ti-doped α-Fe_2O_3 film deposited using 2,000 laser pulses, yielding a film thickness of 22 ± 3 nm (see Supplementary Fig. S6-B). Slightly higher photocurrent densities were obtained using a thicker Ti-doped α-Fe_2O_3 film deposited using 2,500 laser pulses (yielding a film thickness of ~26 nm) and treated with cobalt catalyst[7] before the photoelectrochemical measurements. This photoanode reached 3.02 ± 0.06 mA cm^{-2} at 1.63 V_{RHE} (see Supplementary Fig. S23) and 1.97 ± 0.01 mA cm^{-2} at 1.43 V_{RHE} (Supplementary Fig. S22). The best results were obtained with two of these photoanodes placed facing each other in a 90° V-shaped cell[30] designed to retrap the back-reflected photons (see Supplementary Fig. S21). With this set-up we obtained a photocurrent density of 3.98 ± 0.03 mA cm^{-2} at 1.63 V_{RHE} (see Supplementary Fig. S24). The results are summarized in Fig. 7.

Resonant light trapping in optical cavities comprising semiconductor ultrathin films on back-reflector substrates enables efficient light absorption in quarter-wave or, in some cases, deeper subwavelength films. This approach overcomes the trade-off between light absorption and collection of photogenerated minority charge carriers that limits the solar energy conversion efficiency of semiconductors with poor transport properties. Taking α-Fe_2O_3 photoanodes for water splitting as a case study we predict that as much as 71% of the solar photons of energy above the bandgap energy of α-Fe_2O_3 can be absorbed, at normal incidence, in ultrathin films thinner than 50 nm wherein most of the photogenerated holes can reach the surface and oxidize water before recombination takes place. The escaped back-reflected photons can be harvested by photon retrapping schemes such as using V-shaped cells, thereby further boosting the light-harvesting

efficiency. Water photo-oxidation current densities as high as 4 mA cm^{-2} were obtained under exposure to 100 mW cm^{-2} white-light illumination using Ti-doped α-Fe_2O_3 ultrathin films on silver–gold-coated back reflectors.

The challenge that our light trapping strategy comes to solve and the underlying physical principles are common to other photoelectrode materials, besides α-Fe_2O_3, and other types of solar cell employing semiconductors with poor transport properties. It seems that the enabling key for this strategy to work is strong absorption, as in α-Fe_2O_3. Although some semiconductors such as crystalline Si do not meet this prerequisite, many others do. Therefore, the approach can probably be extended to other materials and systems, opening up new opportunities for employing earth-abundant materials that can be produced potentially at a fraction of the cost of the conventional semiconductors employed in photovoltaics technology at present[37]. Furthermore, shrinking the semiconductor films without compromising their light absorption, enabled by our light trapping strategy, holds promising implications for second-generation thin-film solar cells based on CdTe or $CuIn_{1-x}Ga_xSe_2$ for which the availability of rare-earth elements (Te or In) is a major limitation.

Methods

See Supplementary Information.

Received 21 September 2011; accepted 4 October 2012; published online 11 November 2012

References

1. Bard, A. J. & Fox, M. A. Artificial photosynthesis: Solar splitting of water to hydrogen and oxygen. *Acc. Chem. Res.* **28,** 141–145 (1995).
2. Lewis, N. S. & Nocera, D. G. Powering the planet: Chemical challenges in solar energy utilization. *Proc. Natl Acad. Sci. USA* **103,** 15729–15735 (2006).
3. Walter, M. G. *et al.* Solar water splitting cells. *Chem. Rev.* **110,** 6446–6473 (2010).
4. Fujishima, A. & Honda, K. Electrochemical photolysis of water at a semiconductor electrode. *Nature* **238,** 37–38 (1972).
5. Wrighton, M. S. Photoelectrochemical conversion of optical energy to electricity and fuels. *Acc. Chem. Res.* **12,** 303–310 (1979).
6. Rajeshwar, K. Hydrogen generation at irradiated oxide semiconductor–solution interfaces. *J. Appl. Electrochem.* **37,** 765–787 (2007).
7. Kay, A., Cesar, I. & Grätzel, M. New benchmark for water photooxidation by nanostructured α-Fe_2O_3 Films. *J. Am. Chem. Soc.* **128,** 15714–15721 (2006).
8. Van de Krol, R., Liang, Y. & Schoonman, J. Solar hydrogen production with nanostructured metal oxides. *J. Mater. Chem.* **18,** 2311–2320 (2008).
9. Sivula, K., Le Formal, F. & Grätzel, M. Solar water splitting: Progress using hematite (α-Fe_2O_3) photoelectrodes. *ChemSusChem* **4,** 432–449 (2011).
10. Chen, Z. *et al.* Accelerating materials development for photoelectrochemical hydrogen production: Standards for methods, definitions, and reporting protocols. *J. Mater. Res.* **25,** 3–16 (2010).
11. Brillet, J. *et al.* Examining architectures of photoanode–photovoltaic tandem cells for solar water splitting. *J. Mater. Res.* **25,** 17–24 (2010).
12. Tilley, S. D., Cornuz, M. & Sivula, K. Light-induced water splitting with hematite: Improved nanostructure and iridium oxide catalysis. *Angew. Chem. Int. Ed.* **49,** 6405–6408 (2010).
13. Dare-Edwards, M. P., Goodenough, J. B., Hamnett, A. & Trevellick, P. R. Electrochemistry and photoelectrochemistry of iron(III) oxide. *J. Chem. Soc. Faraday Trans.* **79,** 2027–2041 (1983).
14. Kennedy, J. H. & Frese, K. W. Jr Photooxidation of water at α-Fe_2O_3 electrodes. *J. Electrochem. Soc.* **125,** 709–714 (1978).
15. Wheeler, D. A., Wang, G., Ling, Y., Li, Y. & Zhang, J. Z. Nanostructured hematite: Synthesis, characterization, charge carrier dynamics, and photoelectrochemical properties. *Energy Environ. Sci.* **5,** 6682–6702 (2012).
16. Gärtner, W. W. Depletion layer photoeffects in semiconductors. *Phys. Rev.* **116,** 84–87 (1959).
17. Dotan, H., Sivula, K., Grätzel, M., Rothschild, A. & Warren, S. C. Probing the photoelectrochemical properties of hematite (α-Fe_2O_3) electrodes using hydrogen peroxide as a hole scavenger. *Energy Environ. Sci.* **4,** 958–964 (2011).
18. Upul Wijayantha, K. G., Saremi-Yarahmadia, S. & Peter, L. M. Kinetics of oxygen evolution at α-Fe_2O_3 photoanodes: A study by photoelectrochemical impedance spectroscopy. *Phys. Chem. Chem. Phys.* **13,** 5264–5270 (2011).
19. Pendlebury, S. R. *et al.* Correlating long-lived photogenerated hole populations with photocurrent densities in hematite water oxidation photoanodes. *Energy Environ. Sci.* **5,** 6304–6312 (2012).
20. Klahr, B. M. & Hamann, T. W. Current and voltage limiting processes in thin film hematite electrodes. *J. Phys. Chem. C* **115,** 8393–8399 (2011).
21. Kumar, A., Santangelo, P. G. & Lewis, N. S. Electrolysis of water at $SrTiO_3$ photoelectrodes: Distinguishing between the statistical and stochastic formalisms for electron-transfer processes in fuel-forming photoelectrochemical systems. *J. Phys. Chem.* **96,** 834–842 (1992).
22. Klahr, B. M., Martinson, A. B. F. & Hamann, T. W. Photoelectrochemical investigation of ultrathin film iron oxide solar cells prepared by atomic layer deposition. *Langmuir* **27,** 461–468 (2011).
23. Yablonovitch, E. & Cody, G. D. Intensity enhancement in textured optical sheets for solar cells. *IEEE Trans. Electron Dev.* **29,** 300–305 (1982).
24. Yablonovitch, E. Statistical ray optics. *J. Opt. Soc. Am.* **72,** 899–907 (1982).
25. Bockris, J. O'M. & Uosaki, K. The theory of the light-induced evolution of hydrogen at semiconductor electrodes. *J. Electrochem. Soc.* **125,** 223–227 (1978).
26. Pettersson, L. A. A., Roman, L. S. & Inganäs, O. Modeling photocurrent action spectra of photovoltaic devices based on organic thin films. *J. Appl. Phys.* **86,** 487–496 (1999).
27. Born, M. & Wolf, E. *Principles of Optics* 7th edn (Cambridge Univ. Press, 2010).
28. Formal, F. L., Grätzel, M. & Sivula, K. Controlling photoactivity in ultrathin hematite films for solar water-splitting. *Adv. Funct. Mater.* **20,** 1099–1107 (2010).
29. Murphya, A. B. *et al.* Efficiency of solar water splitting using semiconductor electrodes. *Int. J. Hydrogen Energ.* **31,** 1999–2017 (2006).
30. Rim, S. B., Zhao, S., Scully, S. R., McGehee, M. D. & Peumans, P. An effective light trapping configuration for thin-film solar cells. *Appl. Phys. Lett.* **91,** 243501 (2007).
31. Würfel, P. *Physics of Solar Cells* 2nd edn (Wiley, 2009).
32. Klahr, B., Gimenez, S., Fabregat-Santiago, F., Bisquert, J. & Hamann, T. W. Electrochemical and photoelectrochemical investigation of water oxidation with hematite electrodes. *Energy Environ. Sci.* **5,** 7626–7636 (2012).
33. Hisatomi, T. *et al.* Enhancement in the performance of ultrathin hematite photoanode for water splitting by an oxide underlayer. *Adv. Mater.* **24,** 2699–2702 (2012).
34. Chalmers, B., King, R. & Shuttleworth, R. The thermal etching of silver. *Proc. R. Soc. Lond. Ser. A Math. Phys. Sci.* **193,** 465–483 (1948).
35. Pourbaix, M. *Atlas of Electrochemical Equilibria in Aqueous Solutions* 2nd edn (NACE, 1974).
36. Grätzel, M. Photoelectrochemical cells. *Nature* **414,** 338–344 (2001).
37. Wadia, C., Alivisatos, A. P. & Kammen, D. M. Materials availability expands the opportunity for large-scale photovoltaics deployment. *Environ. Sci. Technol.* **43,** 2072–2077 (2009).

Acknowledgements

This work was supported by the European Commission Seventh Framework Programme (NanoPEC, project 227179), by the I-CORE Program of the Planning and Budgeting Committee and The Israel Science Foundation (grant No. 152/11) and by the KAMIN project from the Office of the Chief Scientist (OCS) in the Ministry of Industry, Trade and Labor (MOITAL). The authors thank S. C. Warren, G. Bartal and N. Tessler for reading the manuscript and providing useful comments and suggestions for improving it.

Author contributions

H.D. and O.K. developed the optical simulation model, and H.D. and A.R. added to it the charge transport model. H.D. designed and fabricated the photoelectrodes and carried out most of the optical and photoelectrochemical measurements. E.S. and O.B. developed the stable silver–gold alloy back reflectors. H.D. and M.G. developed the selective electron transport hole blocking under layers. I.D. carried out the cross-section transmission electron microscope measurements. G.A. carried out the spectroscopic ellipsometry measurements and analysis. A.R. supervised the project and wrote the manuscript. All authors discussed the manuscript and agreed on its final content.

Additional information

Supplementary information is available in the online version of the paper. Reprints and permissions information is available online at www.nature.com/reprints. Correspondence and requests for materials should be addressed to A.R.

Competing financial interests

The authors declare no competing financial interests.

nature materials

SUPPLEMENTARY INFORMATION

DOI: 10.1038/NMAT3477

Resonant light trapping in ultrathin films for water splitting

Hen Dotan[1], Ofer Kfir[2], Elad Sharlin[1], Oshri Blank[1], Moran Gross[1], Irina Dumchin[1], Guy Ankonina[3] and Avner Rothschild [1,*]

[1] Department of Materials Science & Engineering, Technion – Israel Institute of Technology, Haifa, Israel

[2] Physics Department, Technion – Israel Institute of Technology, Haifa, Israel

[3] Photovoltaics Laboratory, Technion – Israel Institute of Technology, Haifa, Israel

* Correspondence should be addressed to AR, e-mail: avnerrot@technion.ac.il

This file includes:

Methods

Supplementary Figures S1 to S27

Supplementary References

DOI: 10.1038/NMAT3477

Methods

Photoelectrode preparation and characterization

Thin film α-Fe_2O_3 photoelectrodes were prepared by pulsed laser deposition (PLD) from a Ti-doped iron oxide target. The target was prepared by the conventional mixed-oxide solid state reaction route, starting from commercial Fe_2O_3 (99.99%) and TiO_2 (99.995%) powders (Alfa Aesar). The powders were mixed in appropriate amounts to obtain a doping level of 1 at% Ti in Fe_2O_3, ball-milled for 24 h using YTZ milling balls (Tosoh, Japan), and subsequently pressed in a stainless steel mold and sintered in air at 1200°C for 12 h, resulting in a target with relative density of 88%.

Thin films were deposited from this target on three different types of substrates: (1) fluorinated tin oxide (FTO) coated glass substrates (TEC15, Pilkington, USA); (2) platinized fused silica substrates (Inostek, South Korea) coated with 150 nm thick platinum layers on top of thin (~10 nm) titanium bonding layers deposited by sputtering on fused silica substrates (ESCO Products, USA); and (3) silver-gold coated glass substrates comprising thick layers of a silver-gold alloy with 90 at% silver and 10 at% gold (unless otherwise mentioned) sandwiched between ultrathin TiN diffusion barrier layers with thin Ti bonding layers deposited by sputtering on Boro-Aluminosilicate glass substrates (Corning Eagle-XG, USA). The TiN films served as diffusion barriers for silver. Schematic cross section illustrations of these structures and photographs of representative specimens are shown in Supplementary Figure S2.

The Ti-doped α-Fe_2O_3 films were deposited using a PLD system equipped with a KrF (λ = 248 nm) excimer laser (COMPexPro 102, Coherent, GmbH). The films were deposited at a laser fluence of 1 J cm^{-2} and repetition rate of 5 Hz, at a target to substrate distance of 70 mm. The depositions on platinized and FTO coated substrates were carried out at a heater setpoint temperature of 600°C, which corresponds to a substrate temperature of approximately 450°C. The films were deposited under oxygen

flow at a pressure of 30 mTorr. Following film deposition the chamber was filled with oxygen to a pressure of 200 Torr, annealed 1 h and subsequently slowly cooled to room temperature. The number of laser pulses was varied between 750 and 15000 pulses to obtain different film thicknesses ranging from 8 to 155 nm, respectively.

The structure of the Ti-doped α-Fe_2O_3 photoanodes on silver-gold coated glass substrates comprised of the following layers, from top to bottom: (1) Ti-doped α-Fe_2O_3 film (deposited by PLD using 2000 or 2500 laser pluses, at a setpoint temperature of 525°C and under oxygen flow at a pressure of 25 mTorr); (2) high-temperature undoped SnO_2 film (deposited by PLD using 250 laser pluses, at a setpoint temperature of 500°C and under oxygen flow at a pressure of 55 mTorr); (3) low-temperature undoped SnO_2 film (deposited by PLD using 100 laser pluses, at a setpoint temperature of 300° and under oxygen flow at a pressure of 25 mTorr); and (4) low-temperature 1 at% Nb-doped SnO_2 film (deposited by PLD using 100 laser pluses, at a setpoint temperature of 300°C in vacuum, ~5×10^{-6} Torr). All films were deposited sequentially, one after the other, without opening the PLD chamber between one deposition and the next one.

The silver-gold coated substrates comprised of Boro-Aluminosilicate glass (Corning Eagle-XG) pieces, approximately 15mm×25mm, on which the following films, from top to bottom, were deposited by sputtering prior to the oxide films depositions (the latter were carried out by PLD in a different chamber): (1) ultrathin (~1 nm) TiN diffusion barrier layer; (2) thick (~1.2 μm) silver-gold reflective layer; (3) thin (~10 nm) Ti bonding layer; (4) thin (~8 nm) TiN diffusion barrier layer; and (5) thin (~10 nm) Ti bonding layer. All metal films were deposited by sputtering, using a Von Ardenne LS320S sputter system, at ambient temperature. The silver-gold layers were deposited by co-sputtering from silver and gold targets (99.99% pure, Kurt J. Lesker, USA) using a DC power source (50 W) for the silver target and an RF power source (15 W) for the gold target. The depositions of the silver-gold layers

DOI: 10.1038/NMAT3477

were carried out for 30 min in an Argon (99.999% Ar, Maxima Gases, Israel) flow of 20 sccm at a pressure of 8 mTorr. The Ti bonding layers were deposited 3 min (each layer) from a titanium target (99.99% pure, Kurt J. Lesker USA) in an Argon flow of 20 sccm (and pressure of 8 mTorr) using an RF power source (138 W). The TiN diffusion barrier layers were deposited from the same titanium target in a mixture of Argon and N_2 (99.999% N_2, Maxima Gases, Israel) flows of 20 sccm for each gas, at a pressure of 20 mTorr, using an RF power source (145 W). The deposition times of the top and bottom TiN layers were 4 and 40 min, respectively. The chamber was evacuated to a base pressure of $\sim 2\times10^{-7}$ Torr prior to the deposition of each layer. Supplementary Figure S3 shows pictures of silver-gold coated substrates in the as-deposited state (i.e., after the sputtering of the metal layers and prior to the PLD of the oxide layers).

The phase composition of the Ti-doped α-Fe_2O_3 films was examined by X-ray diffraction (Philips PW-1820 diffractometer). Exemplary X-ray diffractograms are presented in Supplementary Figure S4. Bragg reflections of the α-Fe_2O_3 (hematite) phase are observed with no other iron or iron oxide phases detected. The chemical composition of three of the films was measured by Rutherford backscattering spectrometry (RBS) using a 5 MV Pelletron accelerator (^{4}He-ions at energy 2 MeV) at the Ångström Laboratory in Uppsala, Sweden. The films were found to have the expected composition with 1 at% Ti. The chemical composition of the silver-gold reflective layers was examined by SEM-EDS and XPS. The layers were found to have the planned (nominal) composition with 90 at% silver and 10 at% gold. Other compositions were also prepared with 5 or 15 at% gold, but in the water photoelectrolysis measurements reported in this work we tested only the 90 at% silver and 10 at% gold alloys. The microstructure of the films was examined by scanning electron microscopy (SEM, FEI E-SEM Quanta 200) and transmission electron microscopy (TEM, FEI Tecnai G^2 T20 S-Twin TEM). The films were flat, smooth and uniform, as demonstrated in Supplementary Figures S5 (SEM, plan view) and S6 (TEM, cross section). No

pinholes were observed. The surface roughness was measured by atomic force microscopy (AFM, XE-100, PSIA Corporation). Films on platinized substrates displayed surface roughness smaller than 1 nm (Ra = 0.7 – 0.8 nm, see Supplementary Figure S7), while films on TEC15 substrates displayed surface roughness of about 9 nm (see Supplementary Figure S8).

Film thickness and optical measurements

The film thickness and optical constants were measured by spectroscopic ellipsometry (VASE Ellipsometer, J. A. Woolam Co., USA). Eight samples were measured; four (750, 1500, 6900 and 15000 laser pulses) on platinized substrates and four (1000, 3000, 5000 and 6900 laser pulses) on TEC15 substrates. The results were analyzed using the optical stack models presented in Supplementary Figure S9. The model for the TEC15 substrates was taken from Ref. S1. The film thicknesses obtained by these analyses are shown in Supplementary Figure S10, and the optical constants in Supplementary Figure S11. From these results (Supplementary Figure S10) we obtained deposition rates of 0.104±0.006 Å per pulse for films deposited on platinized substrates and 0.16±0.04 Å per pulse for films deposited on TEC15 substrates. The latter films displayed considerable surface roughness, in agreement with the AFM results (see Supplementary Figure S8), resulting in some uncertainty in the ellipsometry analysis and in the determination of the film thickness and optical constants. In contrast, films on platinized substrates were smooth (surface roughness < 1 nm), resulting in perfect fittings and very accurate analyses. The thicknesses of the films reported in the article are based on the calibration curves presented in Supplementary Figure S10.

The optical constants of the Ti-doped α-Fe_2O_3 films on platinized substrates were found to be, as expected, independent of the film thickness (see Supplementary Figure S11-A). They are in very good agreement with the values reported in Ref. S2. These values were used in all our optical calculations.

DOI: 10.1038/NMAT3477

The optical constants obtained for Ti-doped α-Fe_2O_3 films on TEC15 substrates are also in fairly good agreement with the values reported in Ref. S2. They display small variance between different films at wavelengths shorter than 450 nm. These unexpected deviations result, most likely, from difficulties in obtaining accurate fittings to the ellipsometry spectra due to the roughness of the TEC15 substrates.

The transmittance (τ) and reflectance (ρ) spectra of the Ti-doped α-Fe_2O_3 specimens on platinized and FTO coated substrates, and one uncoated TEC15 substrate, were measured using a Perkin Elmer Lambda 950 UV/VIS spectrometer equipped with a 150 mm integrating sphere. Exemplary spectra of specimens comprising a 31±3 nm thick Ti-doped α-Fe_2O_3 film on a platinized substrate and a 47±5 nm thick film on a TEC15 substrate are shown in Supplementary Figure S12. The absorptance of specimens on platinized substrates was obtained using the relationships $a_{specimen} = 1 - \rho_{specimen}$. It comprises contributions from both the Ti-doped α-Fe_2O_3 film and the platinum coating, and due to interference effects we cannot extract from these measurements the net absorptance in the Ti-doped α-Fe_2O_3 film. This is done using the optical calculations described in the following.

The net absorptance in Ti-doped α-Fe_2O_3 films on TEC15 substrates was obtained by the following methods, using the transmittance and reflectance spectra measured for specimens with Ti-doped α-Fe_2O_3 films on TEC15 substrates and an uncoated TEC15 substrate (without Ti-doped α-Fe_2O_3 film). In the first method we consider the overall absorptance in the specimen as the sum of the absorptance in the TEC15 substrate and the absorptance in the Ti-doped α-Fe_2O_3 film: $a_{specimen} = a_{substrate} + a_{film} = 1 - \rho_{specimen} - \tau_{specimen}$, where $\rho_{specimen}$ and $\tau_{specimen}$ are the reflectance and transmittance spectra measured for the specimen. Assuming that the substrate absorptance, $a_{substrate}$, is the same as that of an uncoated TEC15 substrate, i.e., $a_{substrate} = a_{TEC15} = 1 - \rho_{TEC15} - \tau_{TEC15}$, the net absorptance in the Ti-doped α-Fe_2O_3 film is $a_{film} = \rho_{TEC15} + \tau_{TEC15} - \rho_{specimen} - \tau_{specimen}$. In the second method we use more elaborate

calculations similar to the ones described in the supporting information of Ref. S3. The details are given is Supplementary Figure S13. This method leads to the following formula for the net absorptance in the Ti-doped α-Fe_2O_3 film: $a_{film} = 1 - \rho_{specimen} - \tau_{specimen}/\tau_{TEC15}$.

The absorptance spectra of the films, $a_{film}(\lambda_0)$, were used to calculate to absorbed photon fluxes presented by the blue circles in Figure 3 of the article, using the formula $I_{abs} = \int_{\lambda_0^{min}}^{\lambda_0^{max}} I_{\lambda_0}^{Sun}(\lambda_0) a_{film}(\lambda_0) d\lambda_0$ wherein $I_{\lambda_0}^{Sun}(\lambda_0) = \lambda_0 (hc)^{-1} E_{\lambda_0}^{Sun}(\lambda_0)$ and $E_{\lambda_0}^{Sun}(\lambda_0)$ is the solar irradiance spectrum (see Ref. S4). The latter was taken from the ASTM G173-03 standard (Ref. S5). The results are presented in Supplementary Figure S14. The experimental results obtained by both methods are quite close to each other, and both of them are in good agreement with the optical calculations. The first method (squares) yields slightly better fitting for the thicker films while the second method (triangles) yields slightly better fitting to the thinner ones. The blue circles in Figure 3 of the article show the average between the values obtained by these methods.

Photoelectrochemical measurements of Ti-doped α-Fe_2O_3 photoanodes on platinized or FTO coated substrates

Photoelectrochemical measurements were carried out, for the most part, in "Cappuccino cells" electrochemical test cells (for more details on the "Cappuccino cells" see Ref. S6) equipped with a potentiostat/galvanostat (Novocontrol Alpha-AK equipped with a POT/GAL electrochemical interface). All measurements were carried out in 1 M NaOH aqueous solution (pH = 13.6). The photoelectrochemical measurements of photoanodes on platinized or FTO coated glass substrates were carried out with pristine Ti-doped α-Fe_2O_3 photoanodes with no catalysts. The current was measured as a function of the electrode potential using a 3-electrode setup with an Ag/AgCl reference electrode and a platinum wire counter electrode. The applied potential was converted to the RHE scale using the Nernst

DOI: 10.1038/NMAT3477

equation. The current density was obtained by dividing the measured current by the electrode area immersed in the electrolyte (0.28 cm^2). This area is also commensurate with the illuminated area of the electrode upon exposure to light.

Current-voltage (*I-V*) measurements in dark and under exposure to white light illumination where carried out at electrode potentials between 0.7 and 1.8 Volts against the reversible hydrogen electrode (V_{RHE}). The applied potential was scanned at a rate of 50 mV/s, cycled back and forth several times to verify that the results are stable (see Supplementary Figure S15). The photocurrent density was obtained by subtracting the dark current from the light current and dividing the result by the illuminated electrode area (0.28 cm^2), see Supplementary Figure S16. The steady state currents in dark and under illumination were monitored using chopped light chronoamperometry measurements, as described in Ref. S7. Exemplary results, measured at electrode potential of 1.4 V_{RHE}, of the champion Ti-doped α-Fe_2O_3 film on a platinized substrate, that is the film deposited using 2500 laser pulses (corresponding to a film thickness of 26±3 nm), are shown in Supplementary Figure S17.

White light illumination was obtained, in all our tests, with a metal halide lamp (150W HQI lamp, Osram) with a color temperature of 4200 K and color rendering index of 85. The light intensity was set to 100 mW cm^{-2} at the position of the "Cappuccino cell" using a reference solar cell (Newport model 91150V reference solar cell and meter, 2 x 2 cm^2, calibrated with fused silica window). We note that our experimental setup is identical, except for the light source, to the setup used in Michael Grätzel lab at EPFL. A reference specimen from EPFL with performance similar to the champion photoanodes reported in Ref. S8 (without the IrO_2 catalyst) measured in our test setup achieved photocurrent densities approximately 10% higher than the results measured, using the same specimen, at EPFL. The difference is, most likely, due to the different spectrum of our light source and the AM1.5G filtered light source at EPFL. We also compared the performance of one of our photoanodes (achieving a photocurrent density

of approximately 1 mA cm^{-2} at 1.63 V_{RHE}) upon exposure to 100 mW cm^{-2} white light illumination obtained with the metal halide lamp used in all our tests and AM1.5G simulated sunlight obtained with a class A solar simulator (ABET 10500 AM1.5G Solar Simulator). The photocurrent densities measured with the metal halide lamp where higher by no more than 5% than their counterparts measured using the solar simulator.

Stability and reflectivity of silver-gold layers

The stability of silver and silver-gold layers with 5, 10 or 15 at% gold was measured in alkaline solutions with 1 M NaOH. Supplementary Figure S18 shows the current measured between electrodes comprising glass substrates coated with silver (red curves) or silver-gold alloy with 5 at% gold (green curves) and a counter electrode comprising platinum wire, measured in 3-electrode setup at electrode potentials between -0.2 and +0.2 vs. an Ag/AgCl reference electrode. The measurements were carried out in the "Cappuccino cell", wherein the electrode area exposed to the electrolyte was 0.28 cm^2. The steady state currents are indicative of corrosion. They are quite significant for the silver electrode, but negligibly small for the silver-gold electrode.

Supplementary Figure S19 shows specular reflectance measurements at an incidence angle of 70° (20° to the surface normal) of fused silica or glass substrates coated with platinum, silver or silver-gold alloys with 5 or 15 at% gold. The reflectance was measured using a spectroscopic ellipsometer (VASE Ellipsometer, J. A. Woolam Co., USA) before (full line curves) and after deposition of Ti-doped α-Fe_2O_3 films using 2200 laser pulses. Measurements inside and outside the α-Fe_2O_3 covered area are shown by short and long dashed curves, respectively. One can see that substrates coated with silver-gold layers are considerably more reflective than platinized substrates at wavelengths larger than 380 or 460 nm for silver-gold alloys with 5 or 15 at% gold, respectively. The silver-gold alloys are much more

DOI: 10.1038/NMAT3477

stable against thermal etching and they do not tarnish as badly as pristine silver upon annealing in the PLD chamber.

Photoelectrochemical measurements of Ti-doped α-Fe_2O_3 photoanodes on silver-gold coated substrates

Photoelectrochemical tests of Ti-doped α-Fe_2O_3 ultrathin film photoanodes on silver-gold (90 at% silver and 10 at% gold) coated glass substrates were carried out in the "Cappuccino cell" setup described above, except for these tests were carried out using an Ivium CompactStat potentiostat/galvanostat rather than the Novocontrol electrochemical system used in the previous measurements. In addition to the standard measurements in the "Cappuchino cell" in which the light stroked the electrode directly at normal incidence, another measurements were carried out in an electrochemical cell designed for testing V-shaped cells designed for retrapping the back reflected photons, as illustrated in Supplementary Figure S20. A picture of the electrochemical cell that was used for testing V-shaped cells is shown in Supplementary Figure S21. In this setup the area of the photoelectrode exposed to the electrolyte ($A_{electrode}$) was approximately 1.45 cm^2 per electrode (that is ~2.9 cm^2 for the two electrodes together) while the aperture area ($A_{aperture}$) that defines the illumination cross section area was 0.196 cm^2. The photocurrent is obtained by dividing the difference between the light current and the dark current by the aperture area, i.e., $J_{photo} = (I_{light} - I_{dark}) / A_{aperture}$.

In addition to measurements of pristine Ti-doped α-Fe_2O_3 photoanodes with no catalysts, we also measured the same photoanodes following surface treatment with cobalt catalyst using the method described in Refs. S9. Chopped light chronoamperometry measurements of pristine (black curves) and cobalt-treated (red curves) Ti-doped α-Fe_2O_3 photoanodes deposited using 2000 or 2500 laser pulses on silver-gold (90 at% silver and 10 at% gold) coated substrates are shown in Supplementary Figures S22.

The thickness of the Ti-doped α-Fe_2O_3 films was 21±2 and 26±3 nm, respectively. The cobalt treatment improved the performance of the thicker Ti-doped α-Fe_2O_3 film, but had little effect on the thinner one. These measurements were carried out in the "Cappuccino cell" setup. Similar measurements were carried out in the electrochemical cell for testing V-shaped cells under direct illumination at normal incidence on the same photoanodes (treated with cobalt catalyst) whose results are shown in Supplementary Figure S22. The results are shown in Supplementary Figure S23. The two setups gave rise to similar results, as expected. Steady state water photo-oxidation current densities as high as 3.0 ± 0.1 mA cm^{-2} were obtained (at electrode potential of 1.63 V_{RHE}) with the thicker Ti-doped α-Fe_2O_3 photoanode treated with cobalt catalyst. The photocurrent density at 1.43 V_{RHE} reached 1.97 ± 0.01 mA cm^{-2}.

In order to capture some of the back reflected photons which, based on our optical calculations, amount to approximately 40% of the intensity of the incident light in case of ultrathin Ti-doped α-Fe_2O_3 films, of the optimal thickness, on silver coated substrates, we placed two photoanodes facing each other in a 90° V-shaped cell, as illustrated schematically in Supplementary Figure S21. Pictures of the two photoanodes and the test setup are given in Supplementary Figure S22. Both photoanodes comprised of ultrathin Ti-doped α-Fe_2O_3 films deposited using 2500 laser pulses on silver-gold coated substrates (with 90 at% silver and 10 at% gold), and they were treated with cobalt catalyst to improve their performance. Exemplary results of chopped light chronoamperometry measurements of these photoanodes obtained at electrodes potentials of 1.43, 1.53 and 1.63 V_{RHE} are shown in supplementary Figure S24. Steady state water photo-oxidation current densities of 2.24 ± 0.01, 3.51 ± 0.03 and 3.98 ± 0.03 mA cm^{-2} were obtained at the respective potentials.

DOI: 10.1038/NMAT3477

The photoanodes remained perfectly stable during multiple tests, displaying reproducible results with no observable changes in color. The champion photoanode was tested many times (more than 20 times) during a period of more than a month, with no degradation in performance.

Optical calculations

In order to calculate the light intensity, that is the squared optical field strength, distribution profile inside the film we take the plane-wave solution of Maxwell's electromagnetic wave equation and tailor it to fit the boundary conditions of the problem with incident solar radiation, at AM1.5G conditions, striking the optical stack illustrated in Figure 1 of the article.

For the case of normal incidence on ideally reflective substrates ($\hat{r}_{23} = -1$) the following expression is obtained for the spectral photon flux (defined as the number of photons per unit time, unit area and unit wavelength) profile inside the film:

$$I_{\lambda_0}(\lambda_0, x) = I_{\lambda_0}^{Sun}(\lambda_0) T(\lambda_0) \left| e^{\frac{2\pi i}{\lambda_0}[n_2(\lambda_0)+i\kappa_2(\lambda_0)]x} - e^{\frac{2\pi i}{\lambda_0}[n_2(\lambda_0)+i\kappa_2(\lambda_0)](2d-x)} \right|^2, \quad \text{(S1a)}$$

$$\text{with} \quad T(\lambda_0) = \frac{n_2(\lambda_0)}{n_1(\lambda_0)} \left| \frac{2n_1(\lambda_0)}{n_1(\lambda_0) + n_2(\lambda_0) + i\kappa_2(\lambda_0) + [n_1(\lambda_0) - n_2(\lambda_0) - i\kappa_2(\lambda_0)] e^{\frac{4i\pi}{\lambda_0}[n_2(\lambda_0)+i\kappa_2(\lambda_0)]d}} \right|^2. \quad \text{(S1b)}$$

$I_{\lambda_0}^{Sun}(\lambda_0)$ is the solar spectral photon flux at AM1.5G conditions, n and κ are the refractive and attenuation indices of the respective media (designated by subscript 1 for water and 2 for α-Fe_2O_3), and the other symbols have their usual meaning.

For comparison we also calculate the spectral photon flux profiles across α-Fe_2O_3 films on transparent substrates ($\hat{r}_{23} = 0$), that is the conventional photoelectrode design. In this case:

$$I_{\lambda_0}(\lambda_0, x) = I_{\lambda_0}^{Sun}(\lambda_0) T(\lambda_0) e^{-\alpha_2(\lambda_0)x}, \quad \text{(S2a)}$$

with $$T(\lambda_0) = \frac{n_2(\lambda_0)}{n_1(\lambda_0)} \left| \frac{2n_1(\lambda_0)}{n_1(\lambda_0) + n_2(\lambda_0) + i\kappa_2(\lambda_0)} \right|^2 \quad \text{(S2b)}$$

the transmissivity at the front surface ($x = 0$), where $\alpha_2(\lambda_0) = 4\pi\kappa(\lambda_0)\lambda_0^{-1}$ is the absorption coefficient of the α-Fe_2O_3 film.

For the general case of partially-reflective metalized substrates with complex refractive indices we use wave summation, $I_{\lambda_0}(\lambda_0, x) \propto \sum \left| E_{\lambda_0, i}(\lambda_0, x) \right|^2$ where $E_{\lambda_0, i}$ is the optical electric field strength (at wavelength λ_0) of the wave in the i'th pass across the film, to obtain the following expression:

$$I_{\lambda_0}(\lambda_0, x) = I_{\lambda_0}^{Sun}(\lambda_0) T(\lambda_0) \left| e^{\frac{2i\pi}{\lambda_0}[n_2(\lambda_0) + i\kappa_2(\lambda_0)]x} + \hat{r}_{23}(\lambda_0) e^{\frac{2i\pi}{\lambda_0}[n_2(\lambda_0) + i\kappa_2(\lambda_0)](2d - x)} \right|^2, \quad \text{(S3a)}$$

with $$T(\lambda_0) = \frac{n_2(\lambda_0)}{n_1(\lambda_0)} \left| \frac{2n_1(\lambda_0)}{n_1(\lambda_0) + n_2(\lambda_0) + i\kappa_2(\lambda_0) - \hat{r}_{23}(\lambda_0)\left[n_1(\lambda_0) - n_2(\lambda_0) - i\kappa_2(\lambda_0)\right] e^{\frac{4i\pi}{\lambda_0}[n_2(\lambda_0) + i\kappa_2(\lambda_0)]d}} \right|^2. \quad \text{(S3b)}$$

$\hat{r}_{23} = (\hat{n}_2 - \hat{n}_3)(\hat{n}_2 + \hat{n}_3)^{-1}$ is the reflection coefficient at the film/substrate interface (i.e., at x = d). The expressions for the extreme cases of ideally reflective or transparent substrates (Eqs. S1 or S2, respectively) are obtained by substituting $\hat{r}_{23} = -1$ or 0, respectively, in Eq. S3.

The reflection coefficients, $\hat{r}_{23}$, were calculated for different film/substrate interfaces between α-Fe_2O_3 and different metal coatings (silver, aluminum, gold and platinum) using the optical constants of the Ti-doped α-Fe_2O_3 films obtained by the spectroscopic ellipsometry measurements (see Supplementary Figure S11) and the optical constants of the respective metals taken from the database of

DOI: 10.1038/NMAT3477

the ellipsometer. The absolute values of $\hat{r}_{23}$ and the phase changes are presented in Supplementary Figure S25.

Supplementary Figures:

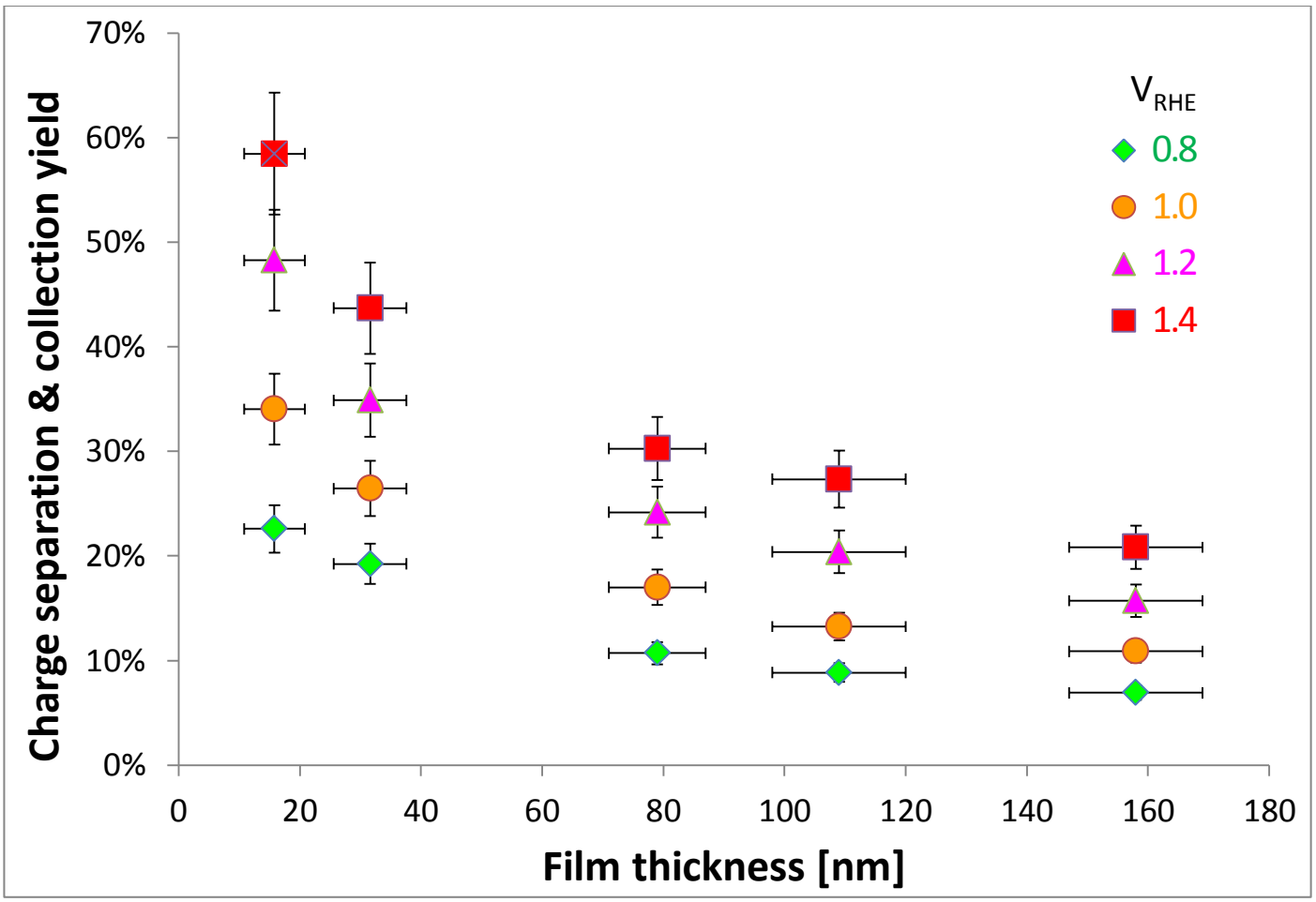

Supplementary Figure S1. The charge separation and collection yield of photogenerated minority charge carriers at the surface of Ti-doped α-Fe_2O_3 thin films deposited by PLD on TEC15 substrates as a function of the film thickness for different applied potentials between 0.8 and 1.4 Volts against the reversible hydrogen electrode (V_{RHE}). The charge separation and collection yield was measured using the method described in Ref. S7.

DOI: 10.1038/NMAT3477

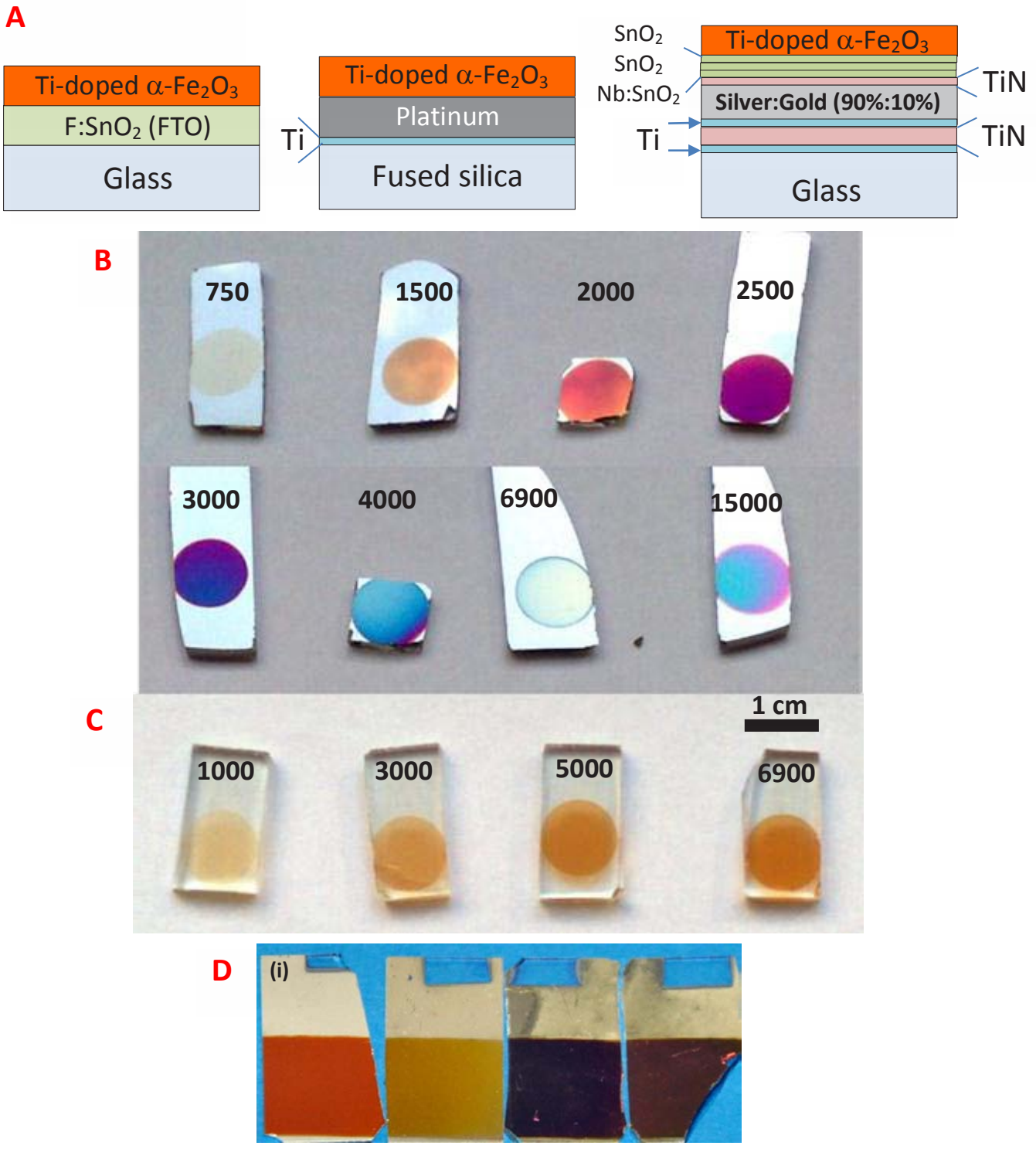

Supplementary Figure S2: Schematic cross section illustrations (A) and photographs of Ti-doped α-Fe_2O_3 films of different thicknesses deposited on platinized (B), TEC15 (C) and silver-gold (90:10) coated glass substrates (D). The number of laser pulses shot at the target is written next to the specimens in Figs. (B) and (C). Sample (i) in Fig. (D) comprises 3 SnO_2 underlayers (100 pulses of Nb-doped SnO_2 deposited in vacuum at 300°C followed by 100 pulses of undoped SnO_2 deposited in 25 mTorr oxygen at 300°C and another 250 pulses deposited in 55 mTorr oxygen at 500°C) on top of which a Ti-doped α-Fe_2O_3 film was deposited in 25 mTorr oxygen at 525°C using 2000 laser pulses. The other specimens in Fig. (D) have other thicknesses of the SnO_2 and α-Fe_2O_3 films.

Supplementary Figure S3: Pictures of a silver-gold (90 at% silver and 10 at% gold) coated glass substrate in the as-deposited (as-sputtered) state (prior to PLD deposition of the oxide layers)

DOI: 10.1038/NMAT3477

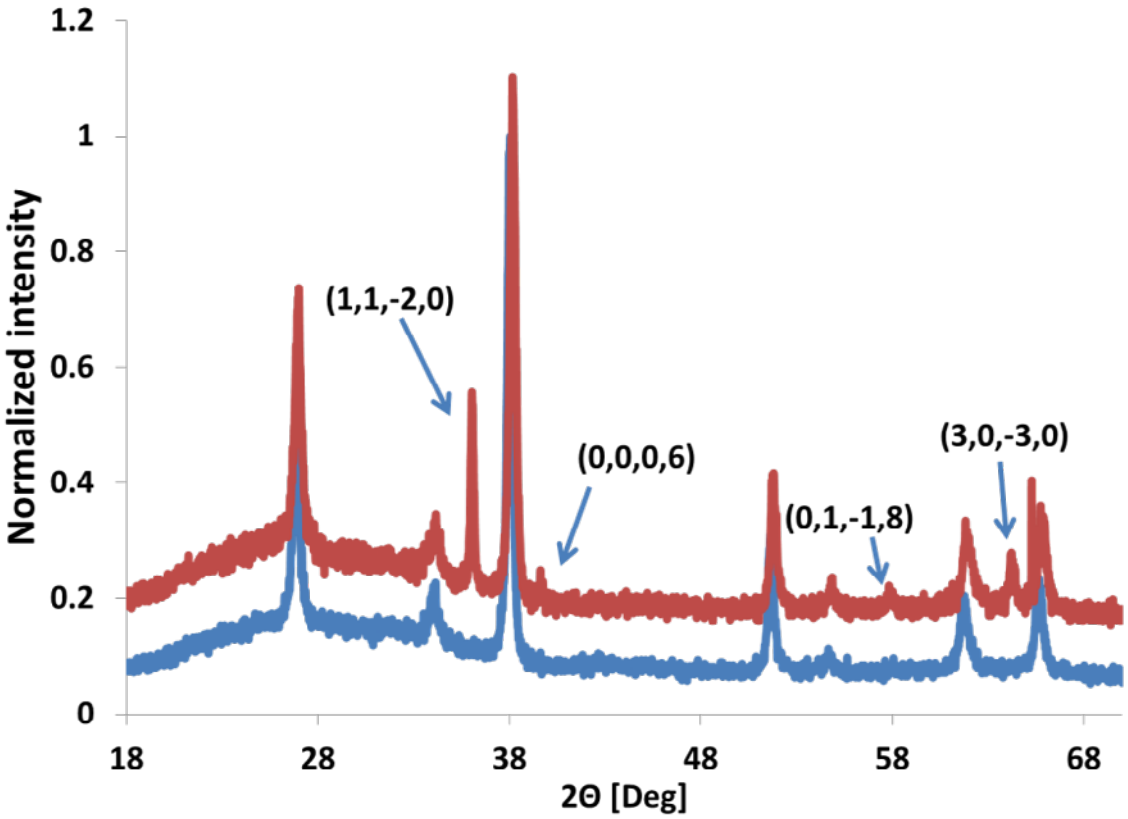

Supplementary Figure S4: XRD diffractograms of a Ti-doped α-Fe_2O_3 film deposited using 20000 laser pulses on a TEC15 substrate (red curve), and an uncoated TEC15 substrate (blue curve). The most prominent Bragg reflections of the α-Fe_2O_3 Hematite structure are marked and their (*hkil*) Miller indices are indicated.

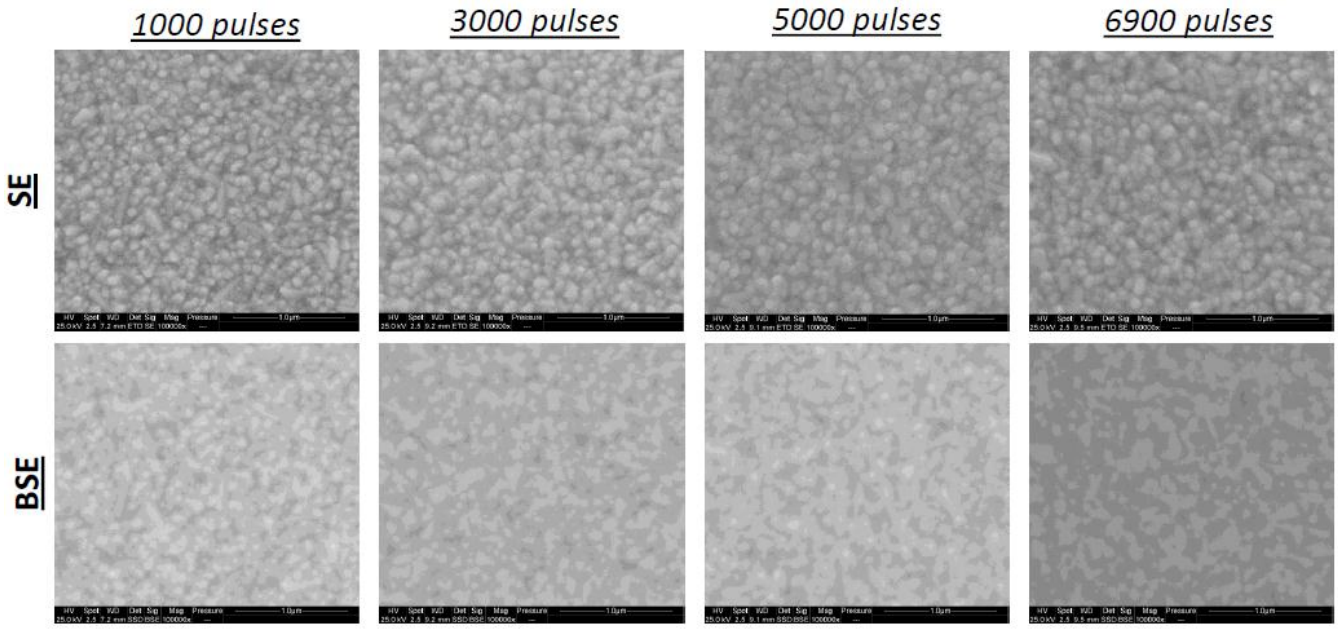

Supplementary Figure S5: Plan view SEM micrographs imaged with secondary electrons (SE) or backscattered electrons (BSE) of Ti-doped α-Fe_2O_3 films deposited using 1000, 3000, 5000 or 6900 laser pulses on TEC15 substrates.

DOI: 10.1038/NMAT3477

A

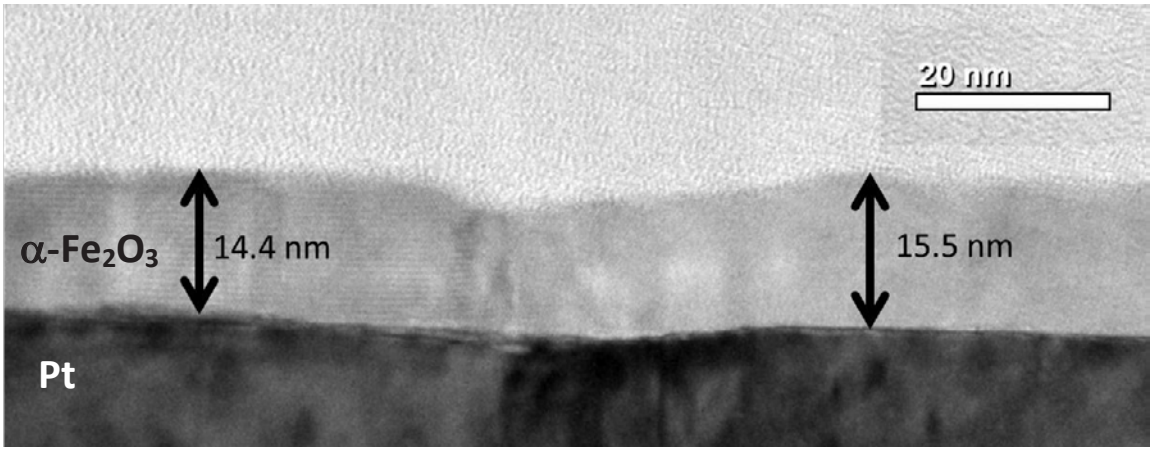

B

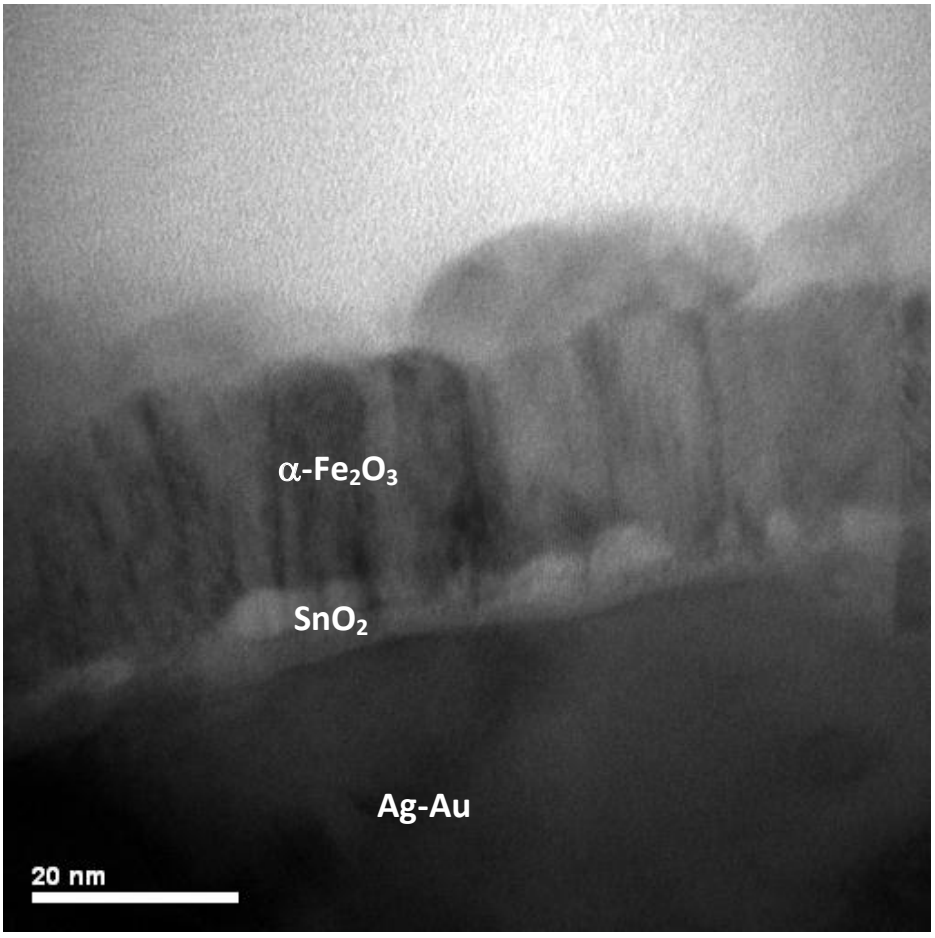

Supplementary Figure S6: Cross section TEM micrographs of Ti-doped α-Fe_2O_3 films deposited on a platinized substrate using 1500 laser pulses (A), or on a silver-gold coated substrate using 2000 laser pulses (B).

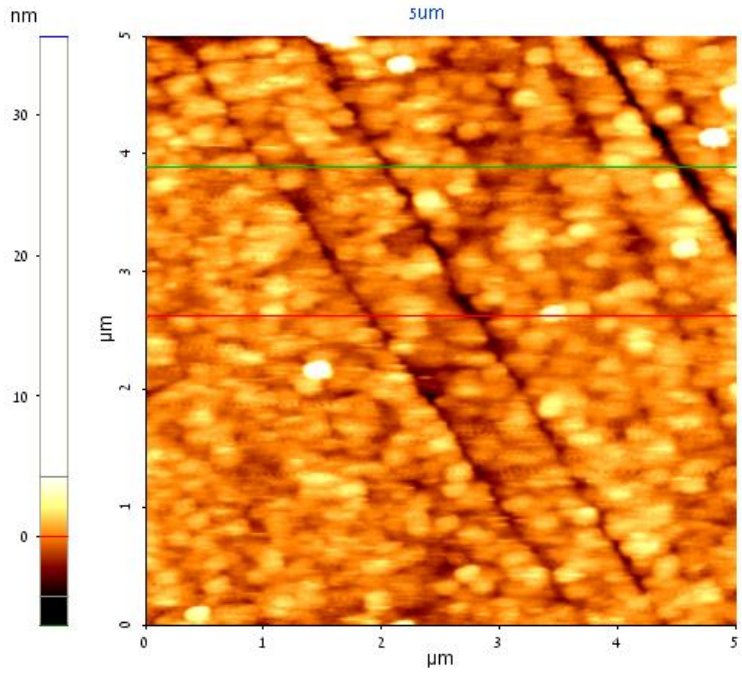

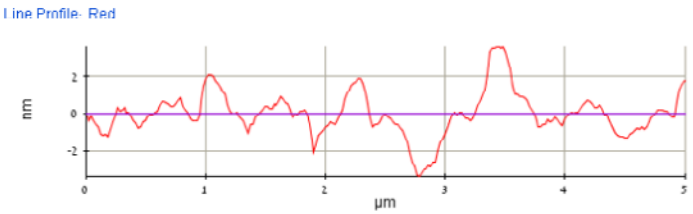

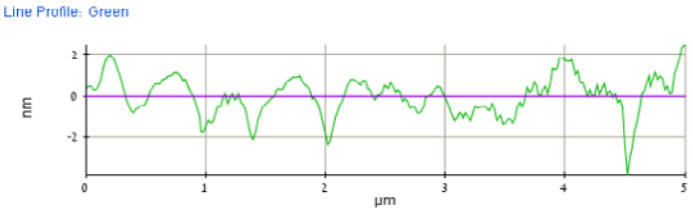

Statistics

Line	Min(nm)	Max(nm)	Mid(nm)	Mean(nm)	Rpv(nm)	Rq(nm)	Ra(nm)	Rz(nm)	Rsk	Rku
Red	-3.340	3.616	0.138	0.001	6.957	1.188	0.823	5.384	-0.339	4.854
Green	-3.767	2.461	-0.653	-0.001	6.228	0.941	0.725	3.888	0.425	3.938

Supplementary Figure S7: AFM micrograph, lines profiles, and line topography statistics of a Ti-doped α-Fe_2O_3 film deposited on a platinized substrate using 3500 laser pulses.

DOI: 10.1038/NMAT3477

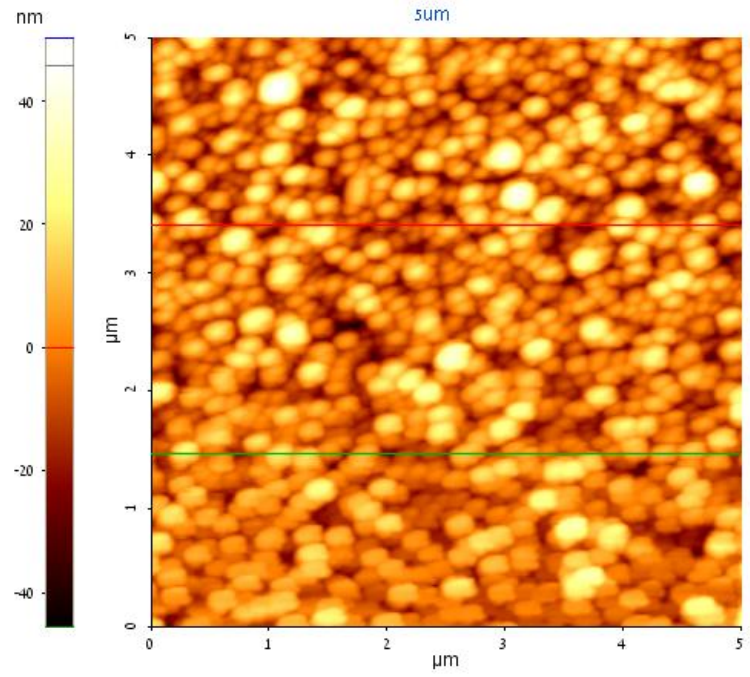

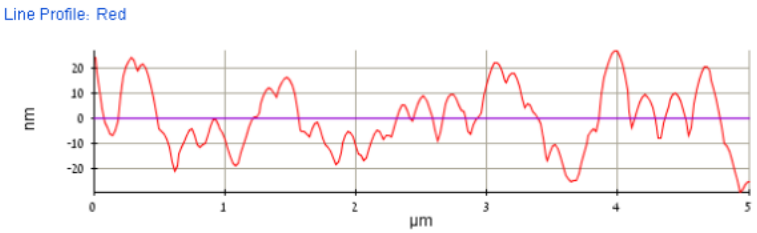

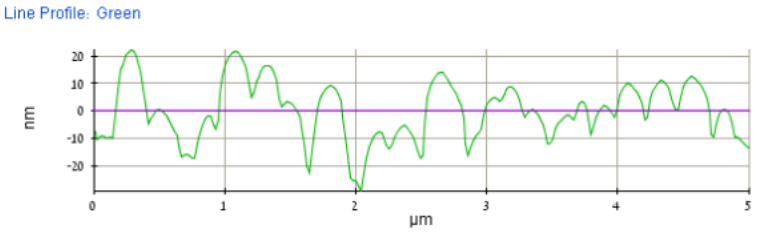

Statistics

Line	Min(nm)	Max(nm)	Mid(nm)	Mean(nm)	Rpv(nm)	Rq(nm)	Ra(nm)	Rz(nm)	Rsk	Rku
Red	-29.384	26.973	-1.205	0.001	56.356	12.627	10.437	45.748	-0.057	2.360
Green	-29.158	22.477	-3.340	0.000	51.635	10.516	8.501	38.224	0.117	2.691

Supplementary Figure S8: AFM micrograph, lines profiles, and line topography statistics of a Ti-doped α-Fe_2O_3 film deposited on a TEC15 substrate using 3000 laser pulses.

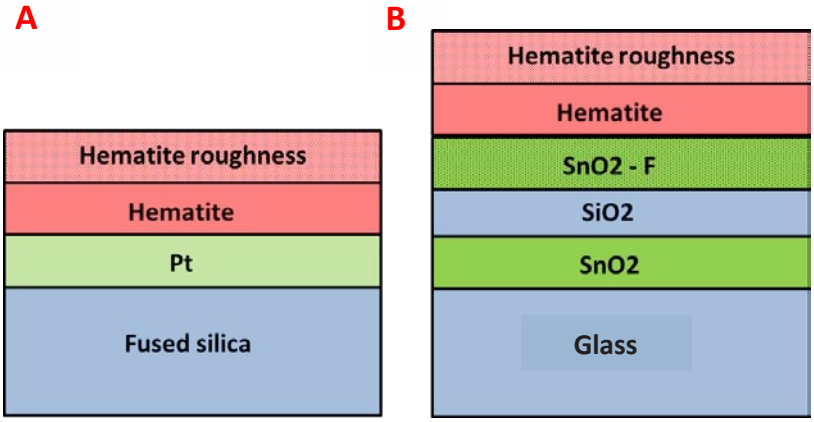

Supplementary Figure S9: Optical stack models used for fitting and analyzing the ellipsometry spectra of Ti-doped α-Fe_2O_3 films on platinized (A) and TEC15 substrates (B).

DOI: 10.1038/NMAT3477

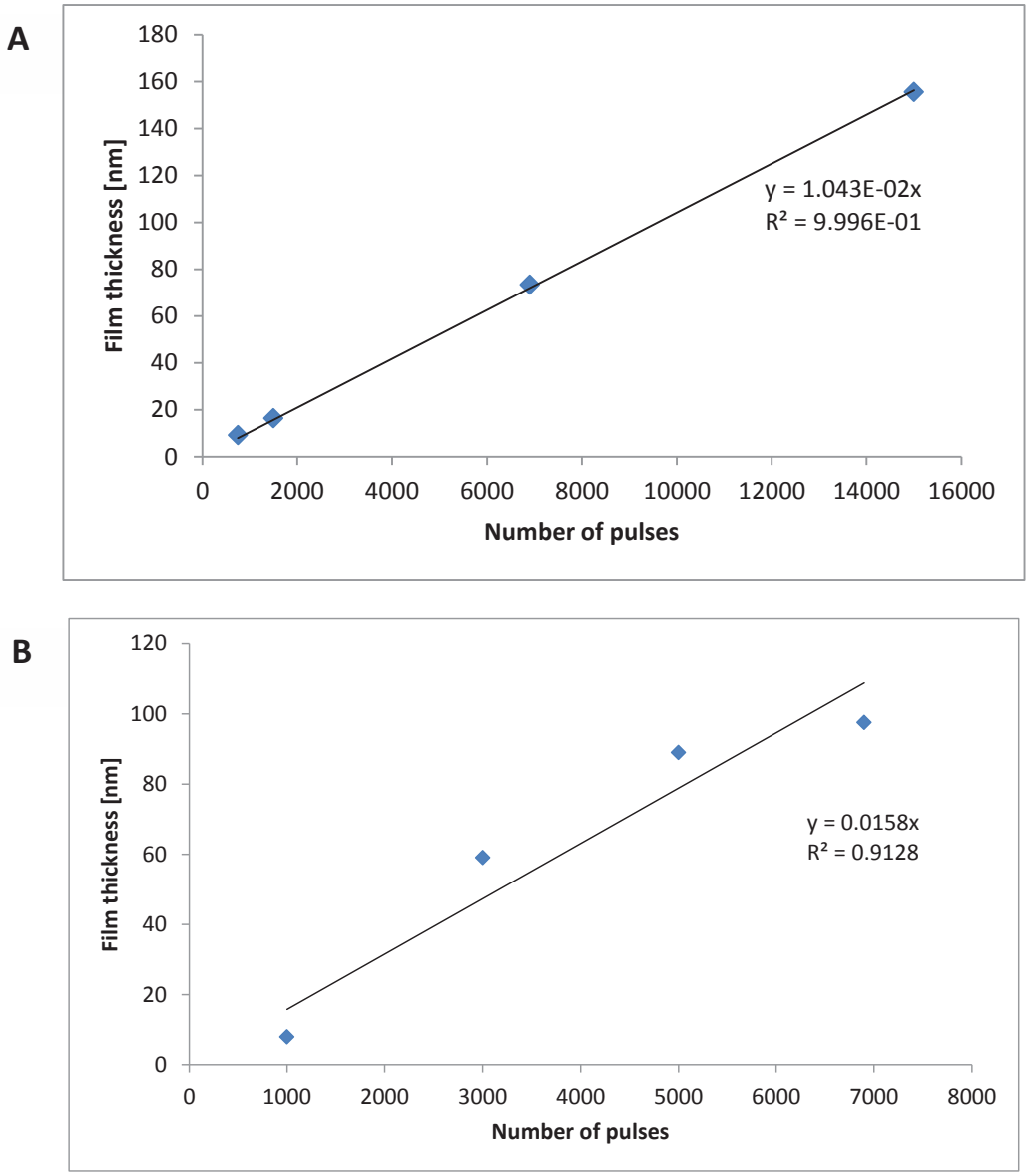

Supplementary Figure S10: Ti-doped α-Fe_2O_3 film thickness as a function of number of laser pulses for films deposited on platinized (A) or TEC15 substrates (B).

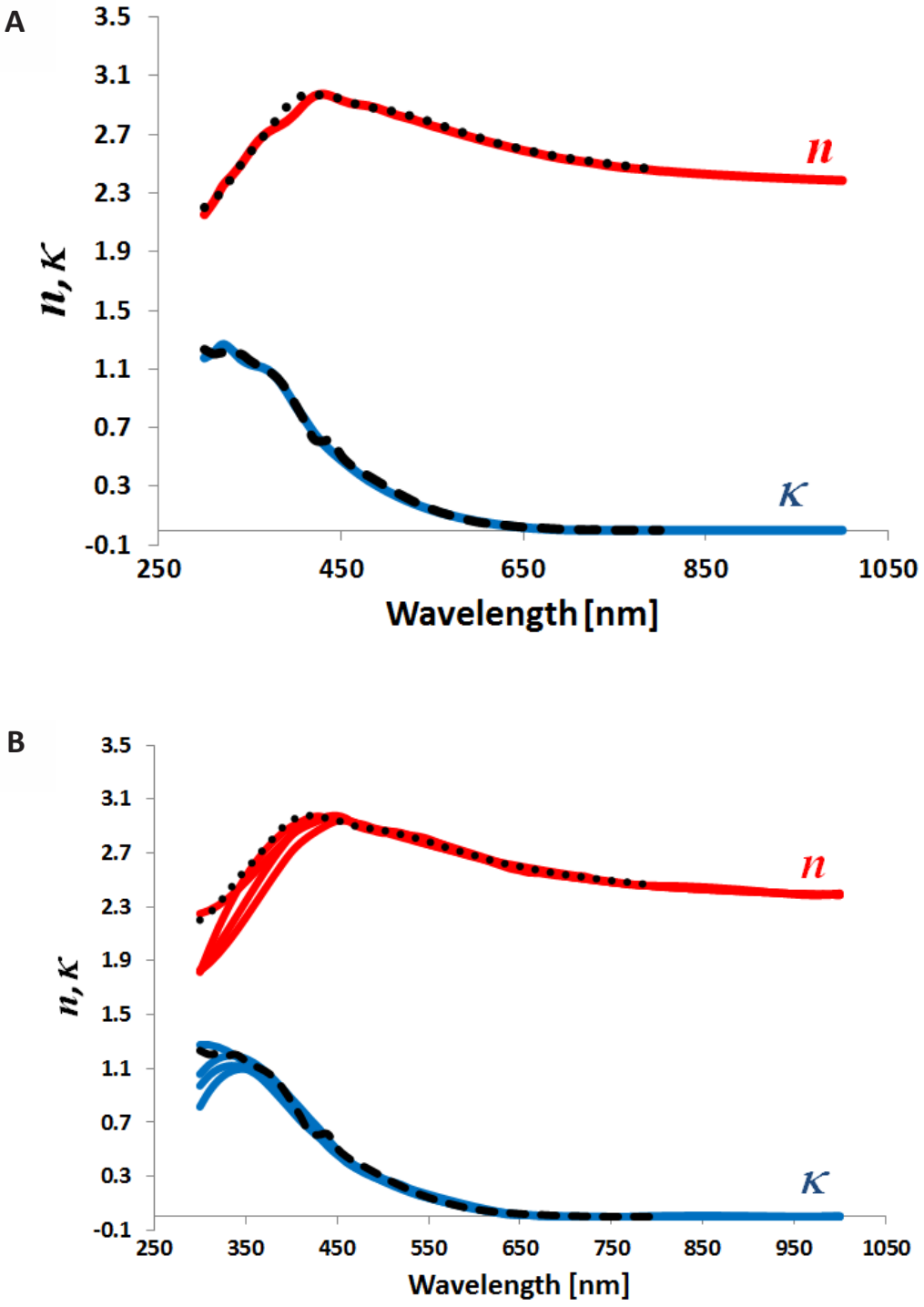

Supplementary Figure S11: The optical constants of Ti-doped α-Fe_2O_3 films deposited on platinized (A) or TEC15 substrates (B). The red and blue lines are the measured n and κ values, respectively, and the black dotted and dashed lines are the respective optical constants reported in Ref. S2.

DOI: 10.1038/NMAT3477

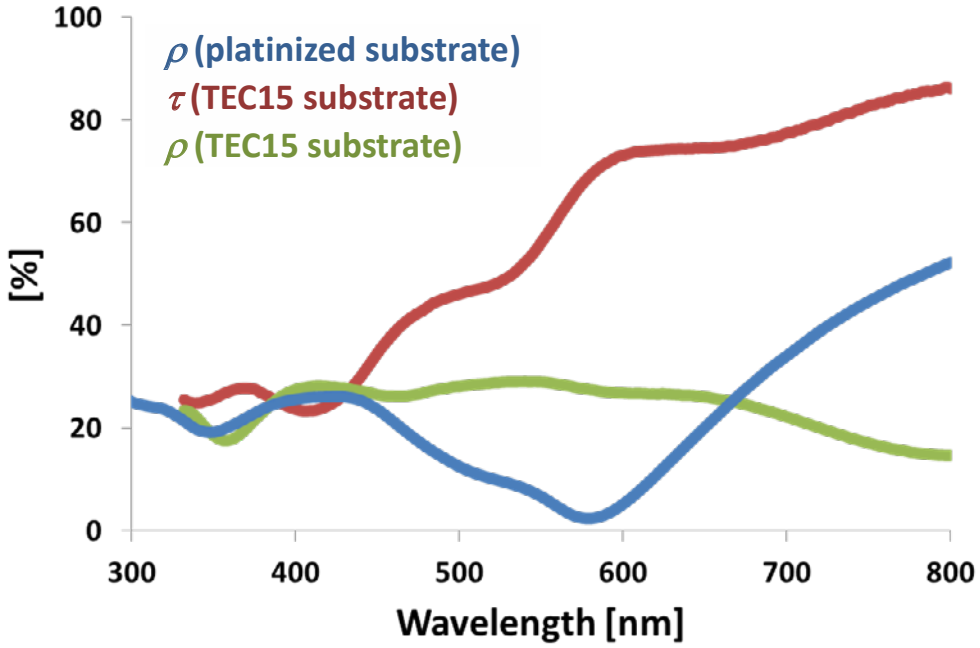

Supplementary Figure S12: Transmittance (τ) and reflectance (ρ) spectra of specimens with a 31±3 nm thick Ti-doped α-Fe_2O_3 film on a platinized substrate or a 47±5 nm thick film on a TEC15 substrate.

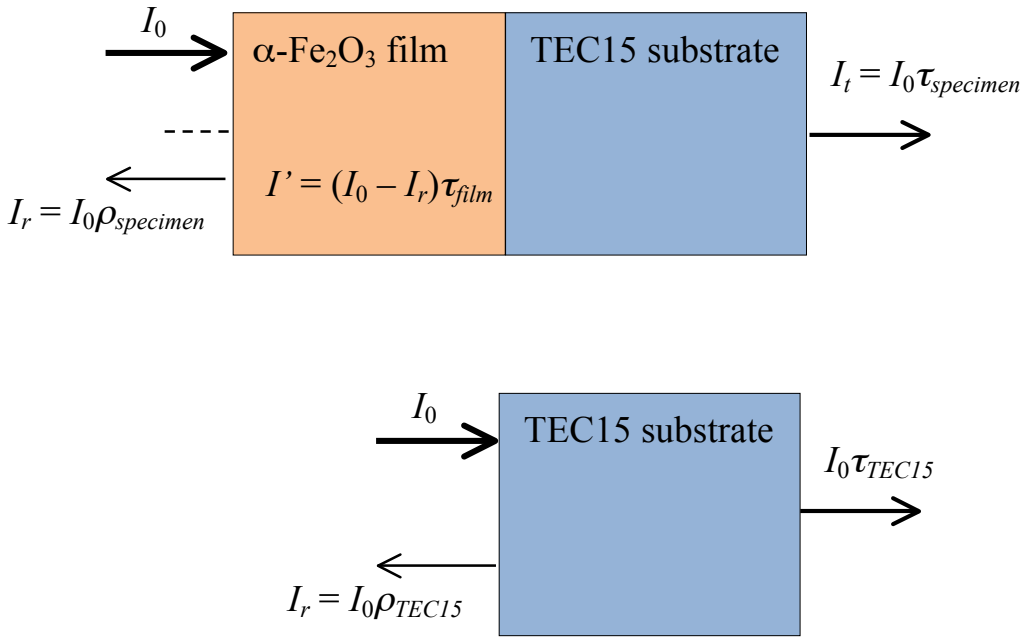

$$I' = (I_0 - I_r)\tau_{film} = I_0(1 - \rho_{specimen})\tau_{film}$$

$$I_t = I_0\tau_{specimen} = I'\tau_{TEC15}$$

$$\rightarrow I' = I_0(\tau_{specimen} / \tau_{TEC15})$$

$$I_0(1 - \rho_{specimen})\tau_{film} = I_0(\tau_{specimen} / \tau_{TEC15})$$

$$\rightarrow \tau_{film} = \tau_{specimen}\,[\tau_{TEC15}\,(1 - \rho_{specimen})]^{-1}$$

$$a_{film} = (1 - \rho_{specimen})(1 - \tau_{film}) = [1 - \rho_{specimen} - (\tau_{specimen} / \tau_{TEC15})]$$

Supplementary Figure S13: Description of the second method used to extract the net absorptance in the α-Fe_2O_3 films from transmittance and reflectance measurements of specimens with Ti-doped α-Fe_2O_3 films on TEC15 substrates and an uncoated TEC15 substrate.

DOI: 10.1038/NMAT3477

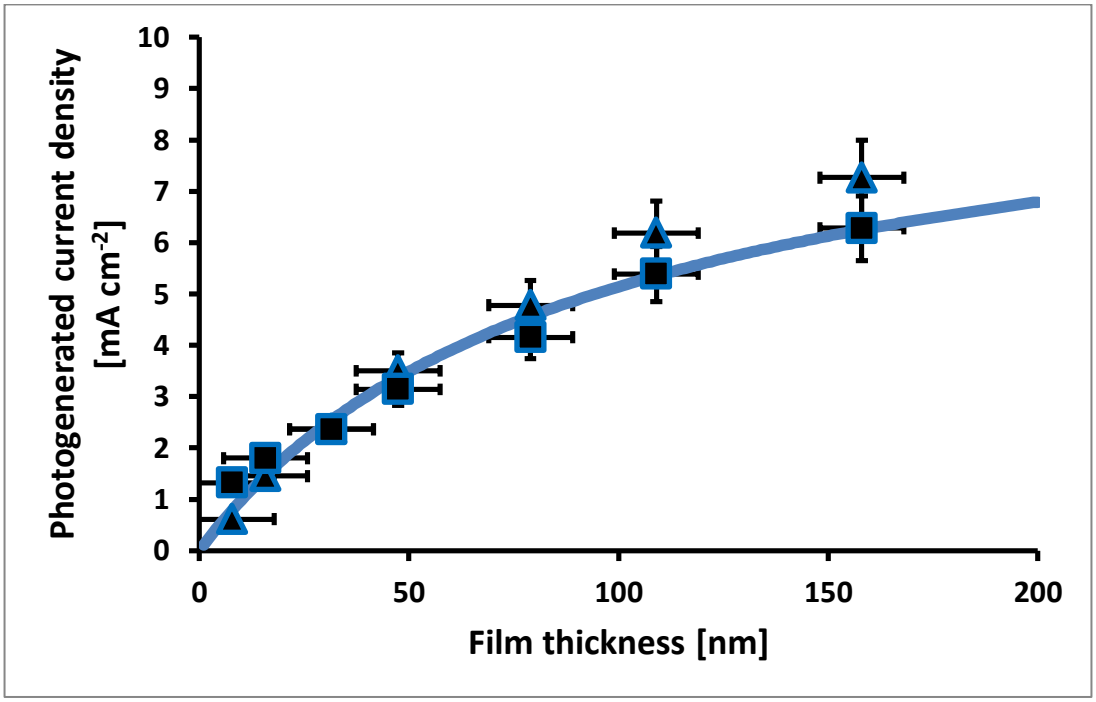

Supplementary Figure S14: The absorbed photon flux, presented in terms of the photogenerated current density, $J_{pg} = qI_{abs}$, obtained by the first (squares) and second (triangles) calculation methods from the transmittance and reflectance spectra of Ti-doped α-Fe_2O_3 films on TEC15 substrates and an uncoated TEC15 substrate. The blue line shows model optical calculations.

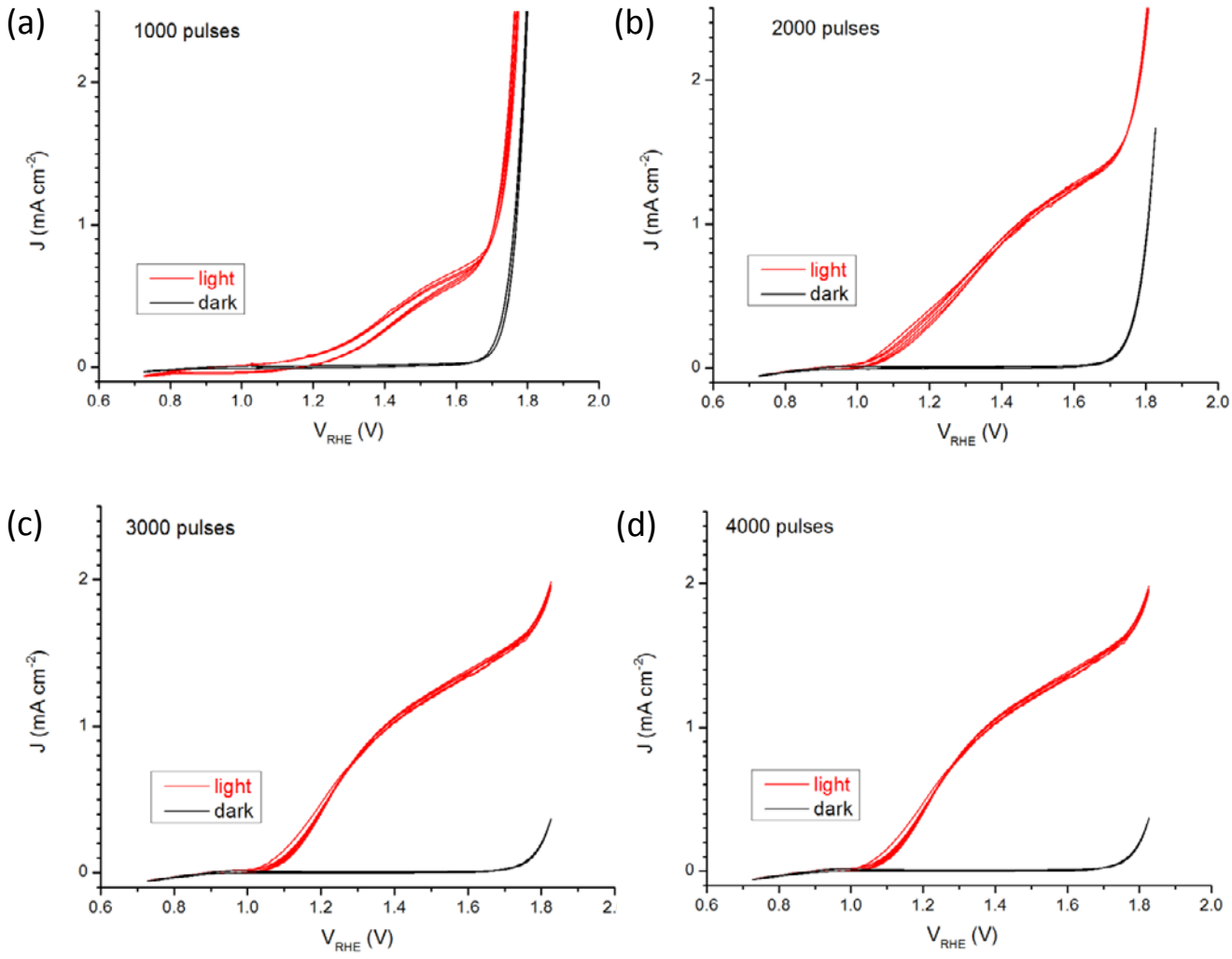

Supplementary Figure S15: Current – voltage characteristics obtained with Ti-doped α-Fe_2O_3 films deposited using (a) 1000, (b) 2000, (c) 3000 or (d) 4000 laser pluses on platinized substrates, measured in 1 M NaOH aqueous solution in dark or under direct illumination (at normal incidence) of white light (100 mW cm^{-2}).

DOI: 10.1038/NMAT3477

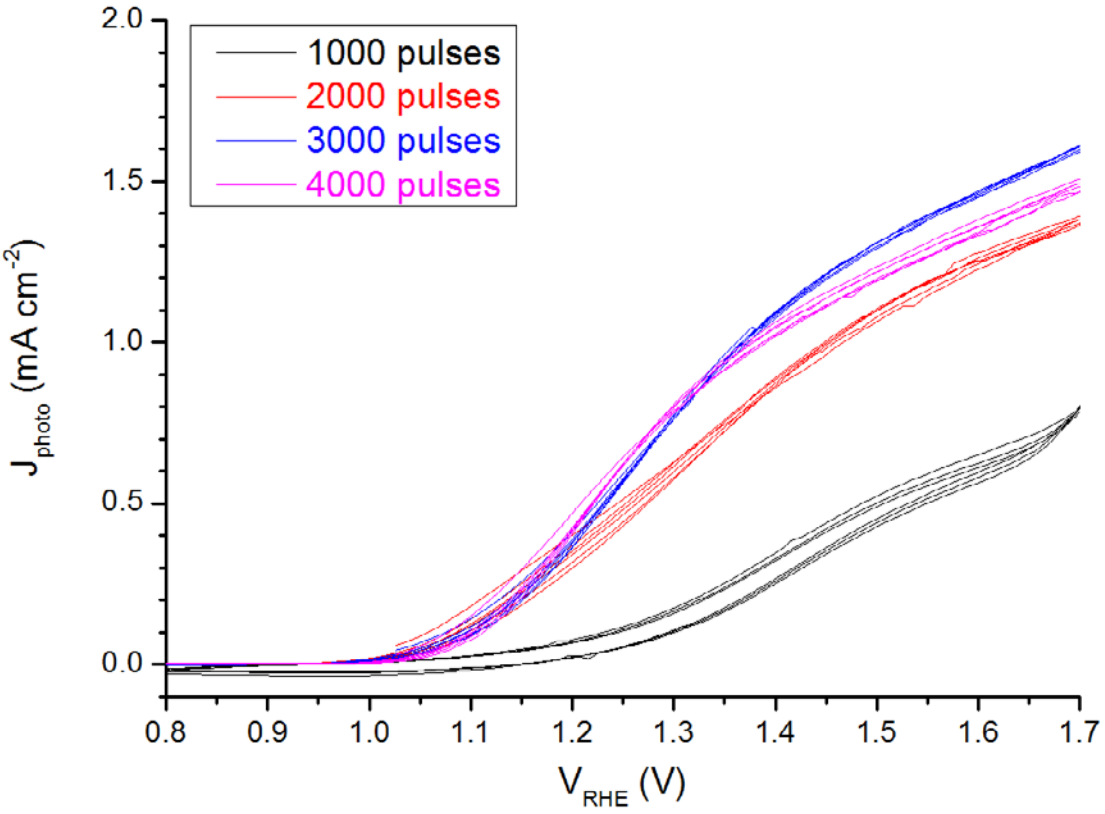

Supplementary Figure S16: Photocurrent ($J_{photo} = J_{light} - J_{dark}$) obtained with Ti-doped α-Fe_2O_3 films deposited using 1000, 2000, 3000 or 4000 laser pluses on platinized substrates.

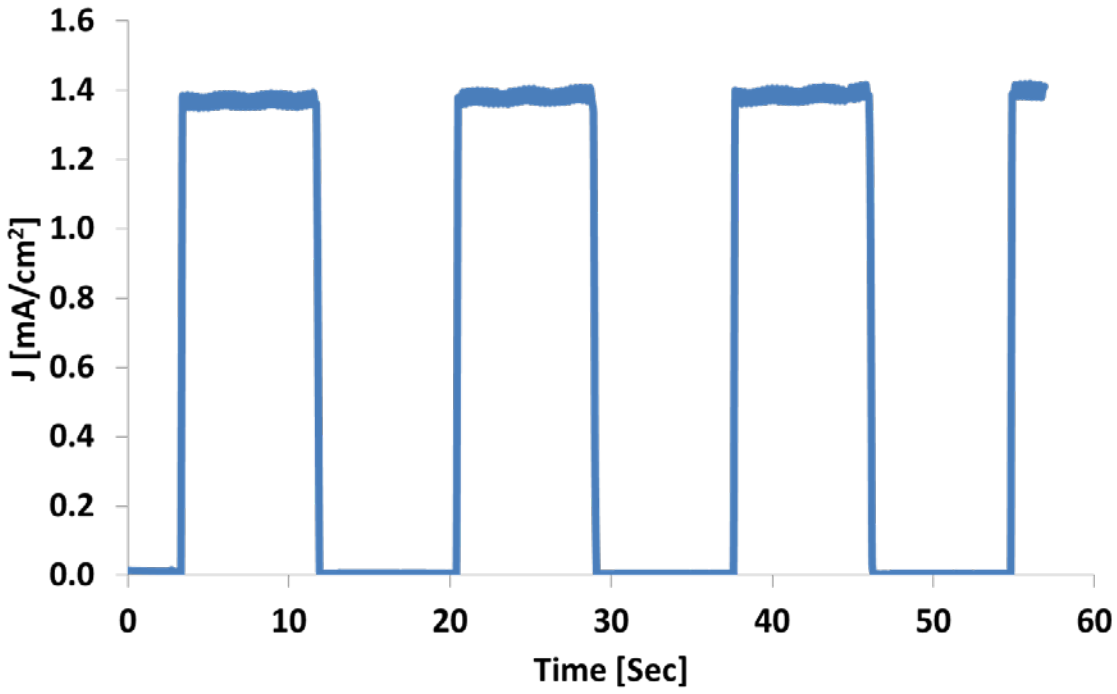

Supplementary Figure S17: Steady state current densities obtained with a 26±3 nm thick Ti-doped α-Fe_2O_3 film deposited using 2500 laser pluses on a platinized substrate, measured at 1.4 V_{RHE} in dark or under illumination during several cycles of chopped light chronoamperometry scans.

DOI: 10.1038/NMAT3477

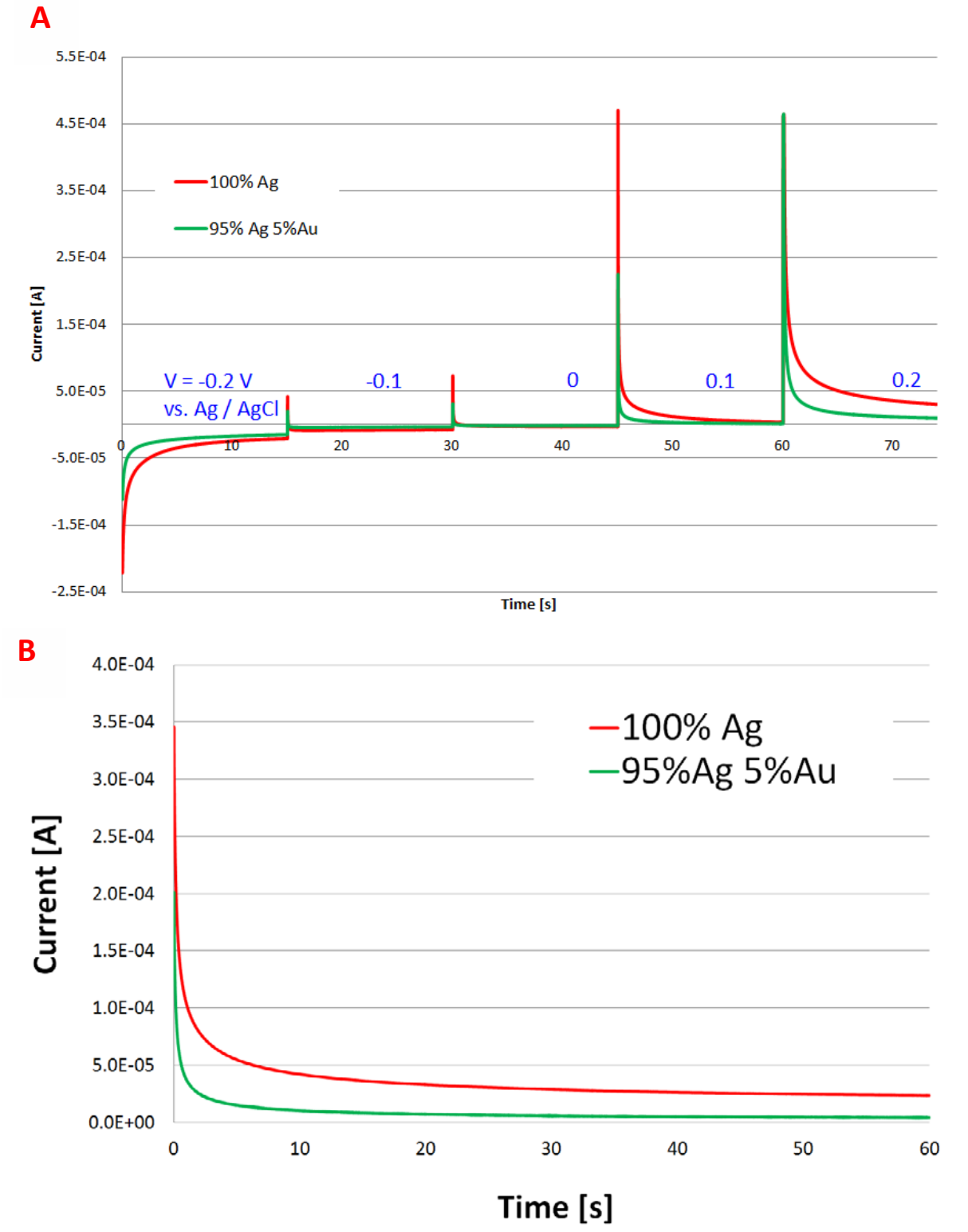

Supplementary Figure S18: Stability tests of glass substrates coated with silver (red curves) or silver-gold alloy with 95 at% silver and 5 at% gold (green curves), in 1 M NaOH solution. Current as a function of time during ramping up the electrode potential from -0.2 to +0.2 V against the Ag/AgCl reference electrode (A); and during applying a potential of +0.2 V against the Ag/AgCl reference electrode (B).

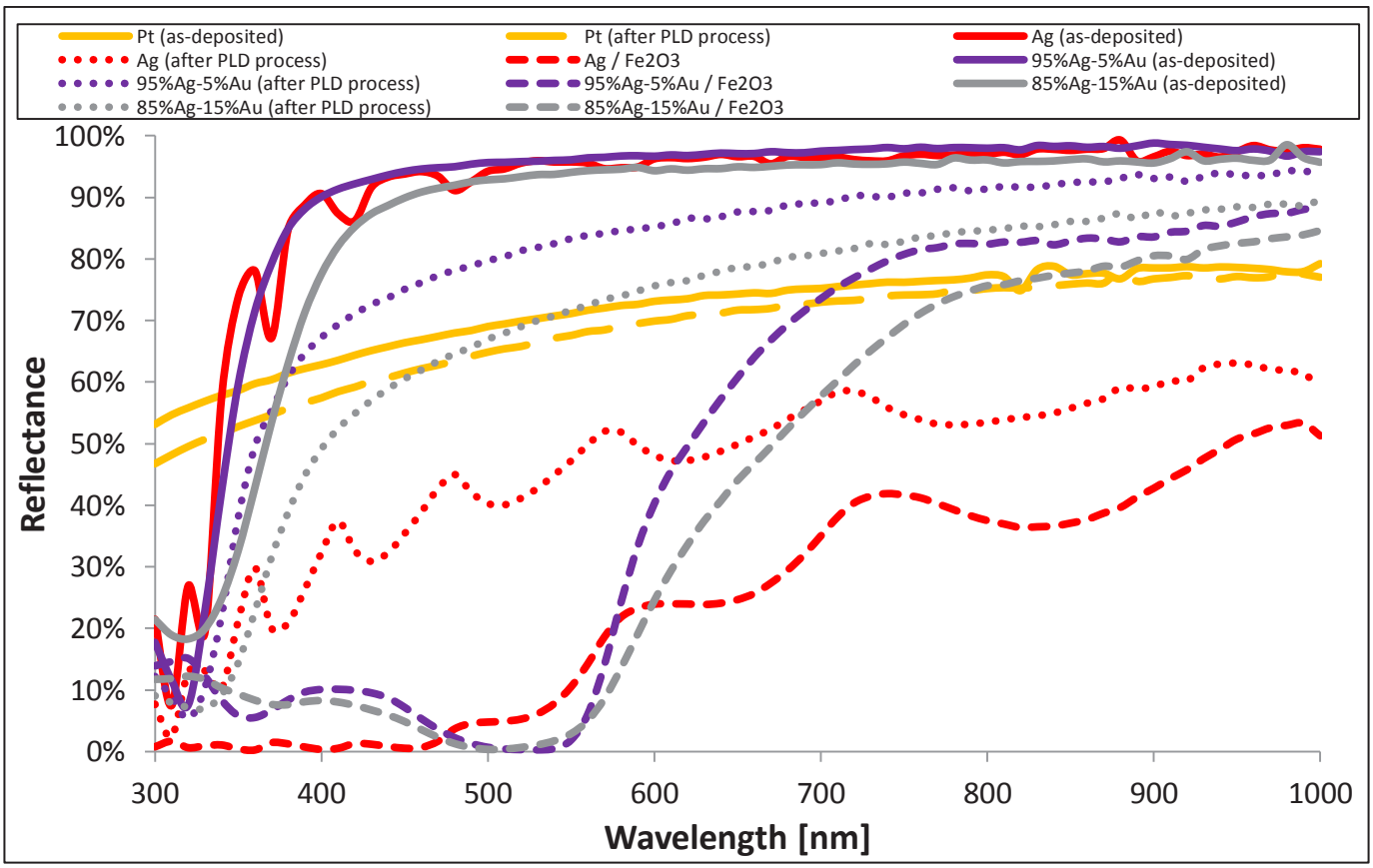

Supplementary Figure S19: Specular reflectance measurements of fused silica or glass substrates coated with platinum (yellow curves), silver (red curves) or silver-gold alloys with 5 (purple curves) or 15 at% gold (grey curves), measured before (full line curves) and after deposition of Ti-doped α-Fe_2O_3 films inside (dashed curves) or outside (dotted curves) the α-Fe_2O_3 covered area. Note that the oscillations in the silver coated substrate are due to the small thickness of the silver layer in this particular specimen. All other specimens had much thicker metal layers.

DOI: 10.1038/NMAT3477

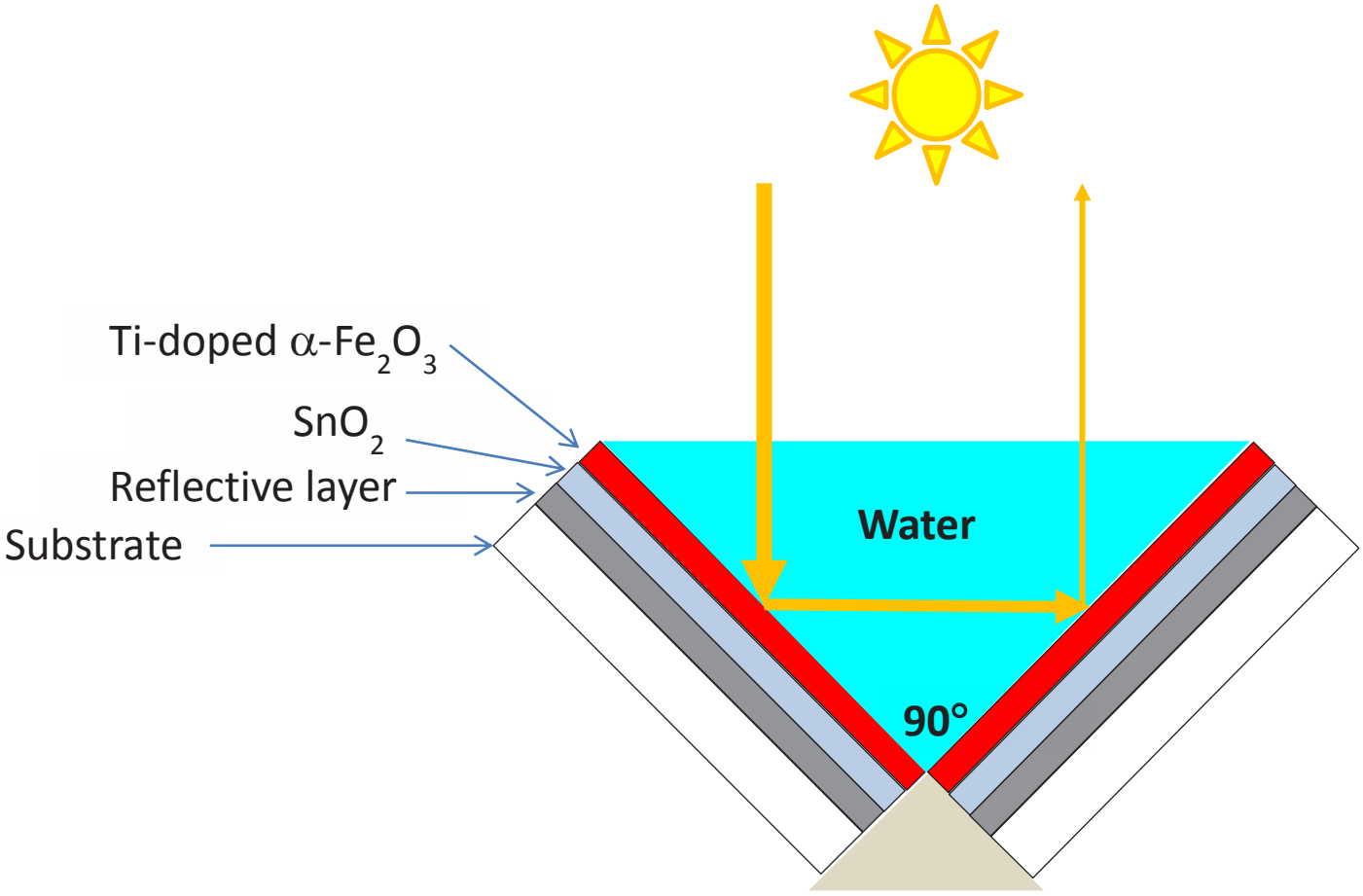

Supplementary Figure S20: Schematic illustration of photon retrapping using a 90° V-shaped cell.

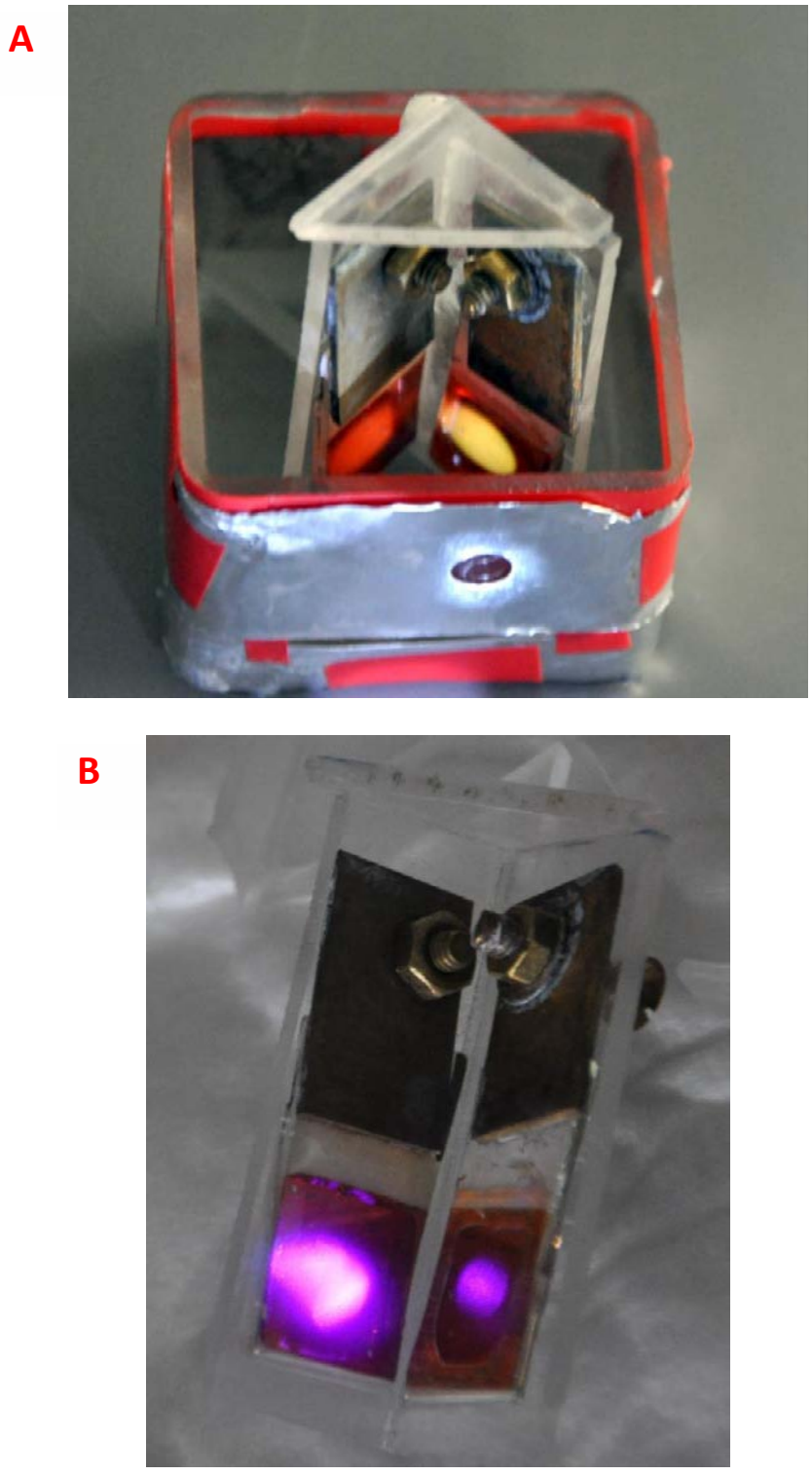

Supplementary Figure S21: Pictures of the electrochemical cell for testing V-shaped cells (A), and a V-shaped cell comprising ultrathin Ti-doped α-Fe_2O_3 films deposited using 2500 laser pulses on silver-gold coated glass substrates faced at 90° against each other (B).

DOI: 10.1038/NMAT3477

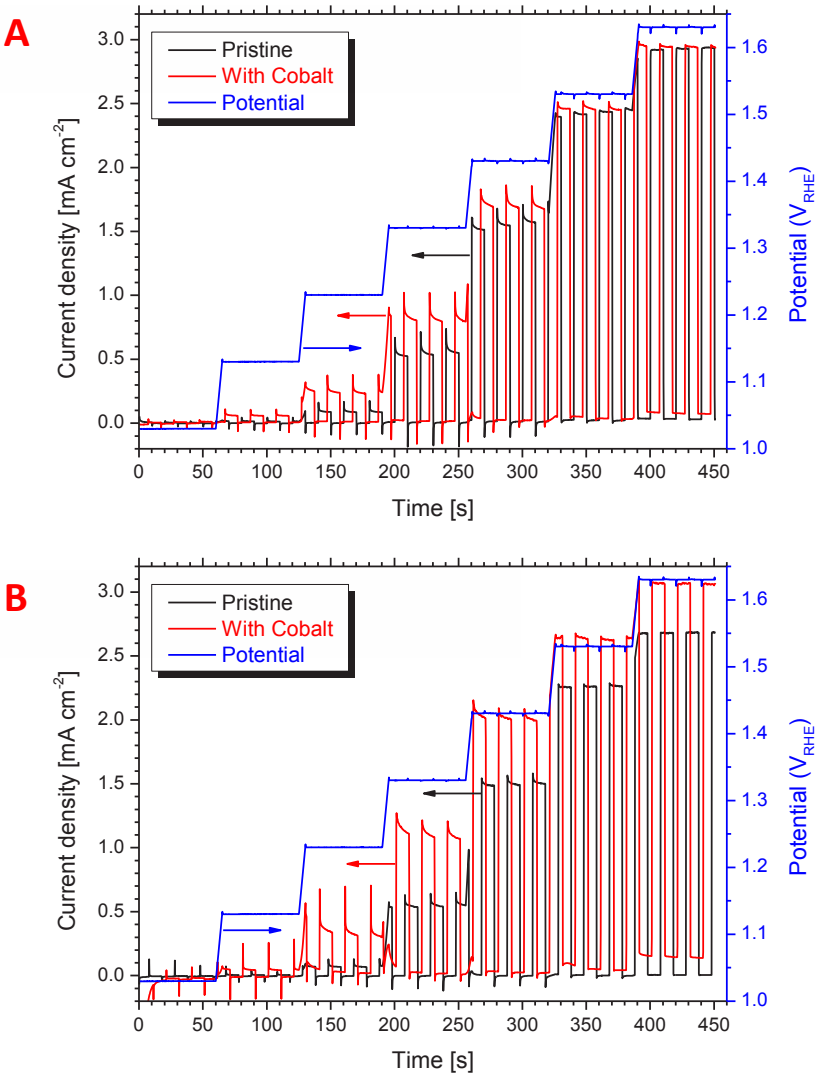

Potential [V_{RHE}]	J_{photo} [mA cm^{-2}]			
	2000 laser pulses		2500 laser pulses	
	Pristine	With Cobalt	Pristine	With Cobalt
1.23 ± 0.01	0.085 ± 0.001	0.225 ± 0.006	0.069 ± 0.001	0.30 ± 0.01
1.33 ± 0.01	0.53 ± 0.01	0.782 ± 0.004	0.538 ± 0.003	1.06 ± 0.02
1.43 ± 0.01	1.55 ± 0.02	1.659 ± 0.005	1.492 ± 0.007	1.97 ± 0.01
1.53 ± 0.01	2.40 ± 0.01	2.412 ± 0.006	2.255 ± 0.005	2.58 ± 0.01
1.63 ± 0.01	2.90 ± 0.01	2.866 ± 0.003	2.677 ± 0.002	2.93 ± 0.02

Supplementary Figure S22: Chopped light chronoamperometry measurements obtained with Ti-doped α-Fe_2O_3 photoanodes deposited using 2000 (A) or 2500 (B) laser pulses on silver-gold coated substrates, in the pristine state (i.e., without a catalyst, black curves) and after treatment with cobalt catalyst (red curves). The applied potential is shown by the blue curves with reference to the right axis. The measurements were carried out in a "Cappuccino cell" under cyclic exposure to dark / light cycles.

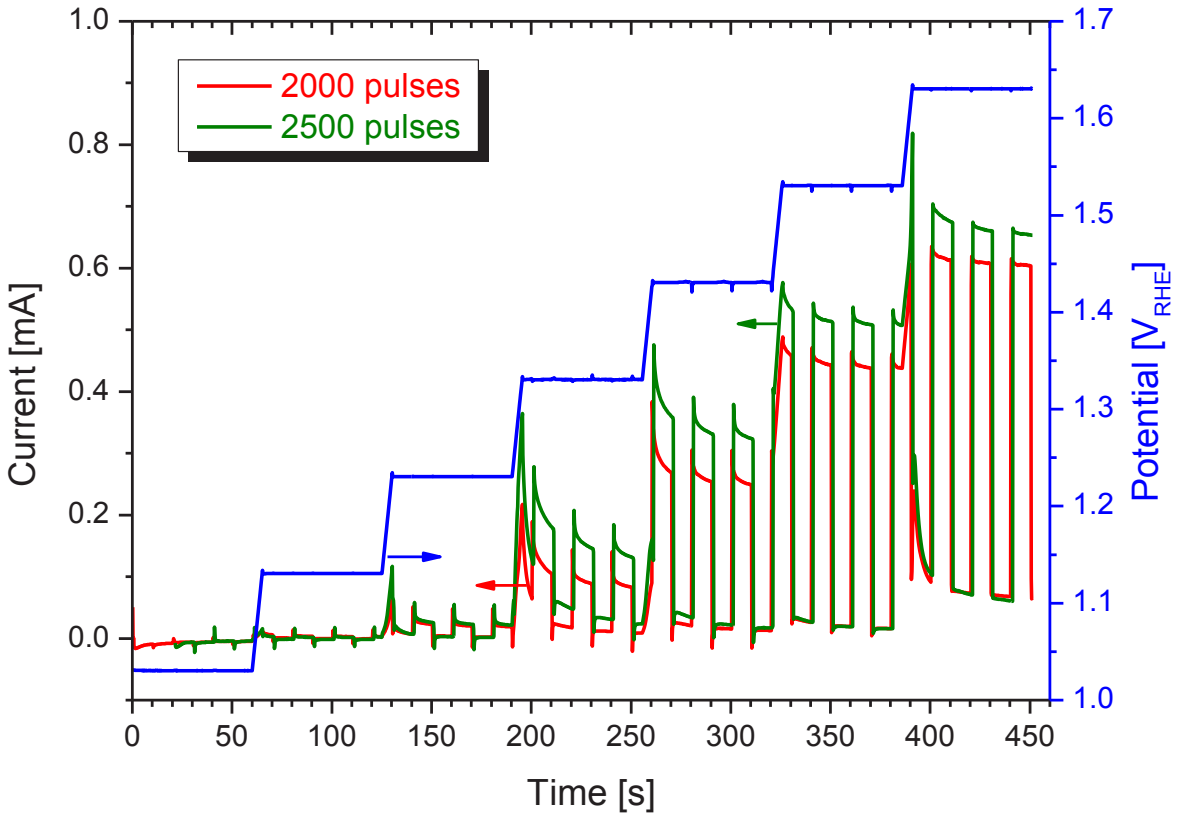

Potential [V_{RHE}]	$J_{photo} = \Delta I / A_{apertute}$ [mA cm^{-2}]	
	2000 laser pulses	**2500 laser pulses**
1.23 ± 0.01	0.09 ± 0.01	0.11 ± 0.01
1.33 ± 0.01	0.38 ± 0.02	0.50 ± 0.05
1.43 ± 0.01	1.20 ± 0.01	1.53 ± 0.03
1.53 ± 0.01	2.16 ± 0.03	2.51 ± 0.03
1.63 ± 0.01	2.73 ± 0.04	3.02 ± 0.06

Supplementary Figure S23: Chopped light chronoamperometry measurements obtained with Ti-doped α-Fe_2O_3 photoanodes deposited using 2000 (red curve) or 2500 (green curve) laser pulses on silver-gold coated substrates and treated with cobalt catalyst. The applied potential is shown by the blue curve with reference to the right axis. The measurements were carried out in the electrochemical test cell whose picture is shown in Supplementary Figure S21-A, but in these tests the photoanodes were illuminated directly (i.e., at normal incidence) without forming the V shape as in Supplementary Figure S21-B.

DOI: 10.1038/NMAT3477

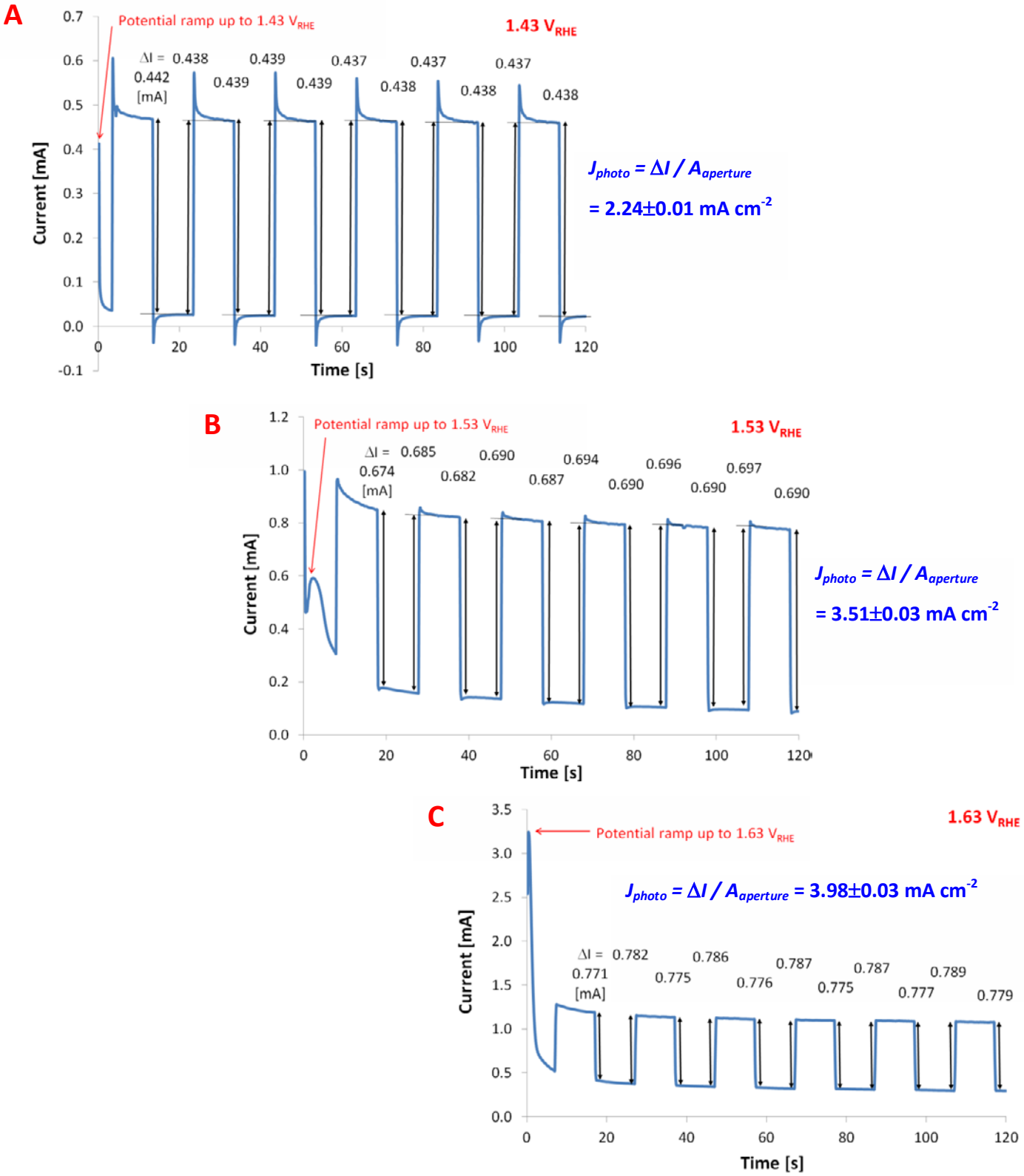

Supplementary Figure S24: Chopped light chronoamperometry measurements obtained with Ti-doped α-Fe_2O_3 photoanodes deposited using 2500 pulses on silver-gold coated substrates and treated with cobalt catalyst, measured in a 90° V-shaped cell configuration at 1.43 (A), 1.53 (B) and 1.63 V_{RHE} (C).

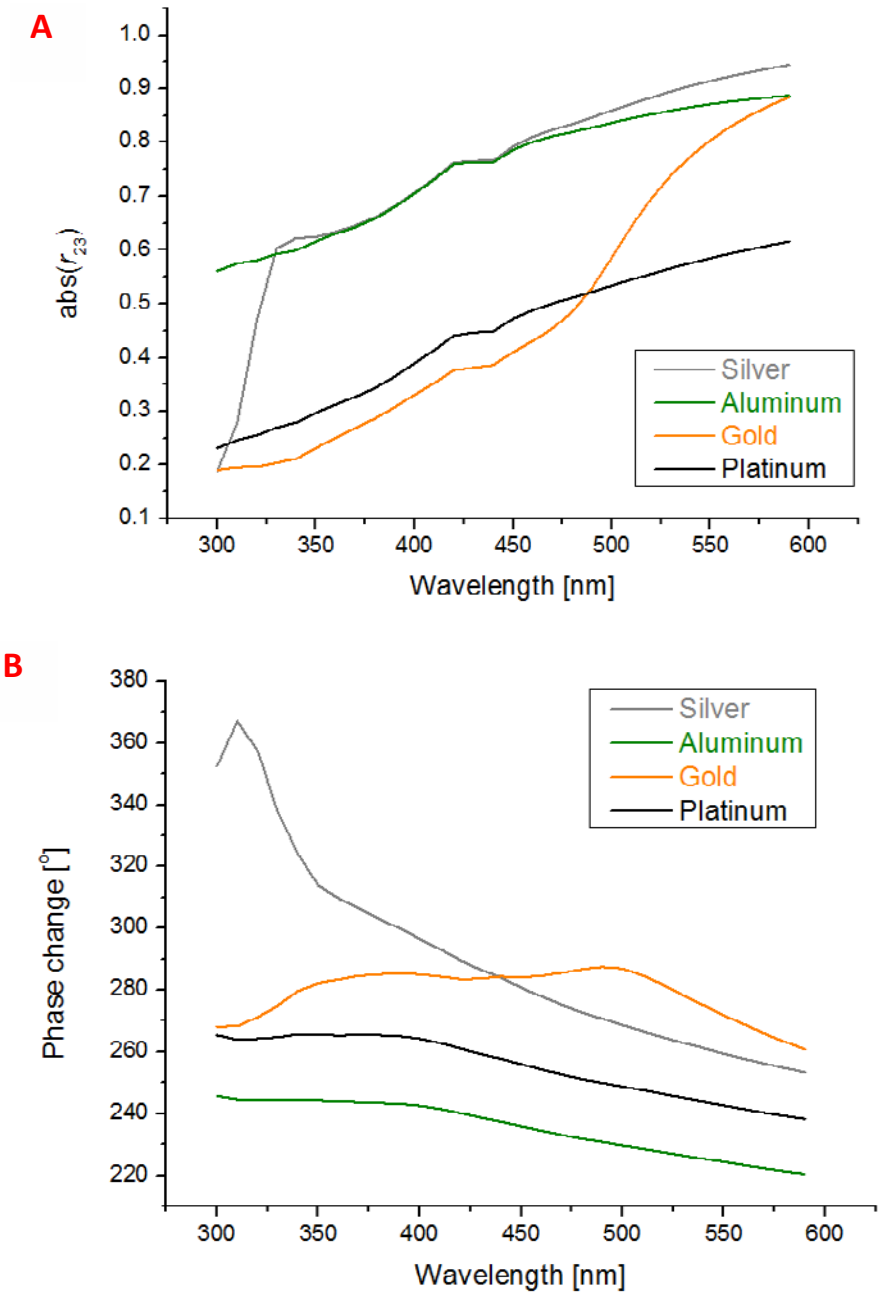

Supplementary Figure S25: The predicted absolute value of $\hat{r}_{23}$ (A) and phase change (B) for reflection from Ti-doped α-Fe_2O_3/metal interfaces with silver (grey), aluminum (yellow), gold (orange) and platinum (black).

DOI: 10.1038/NMAT3477

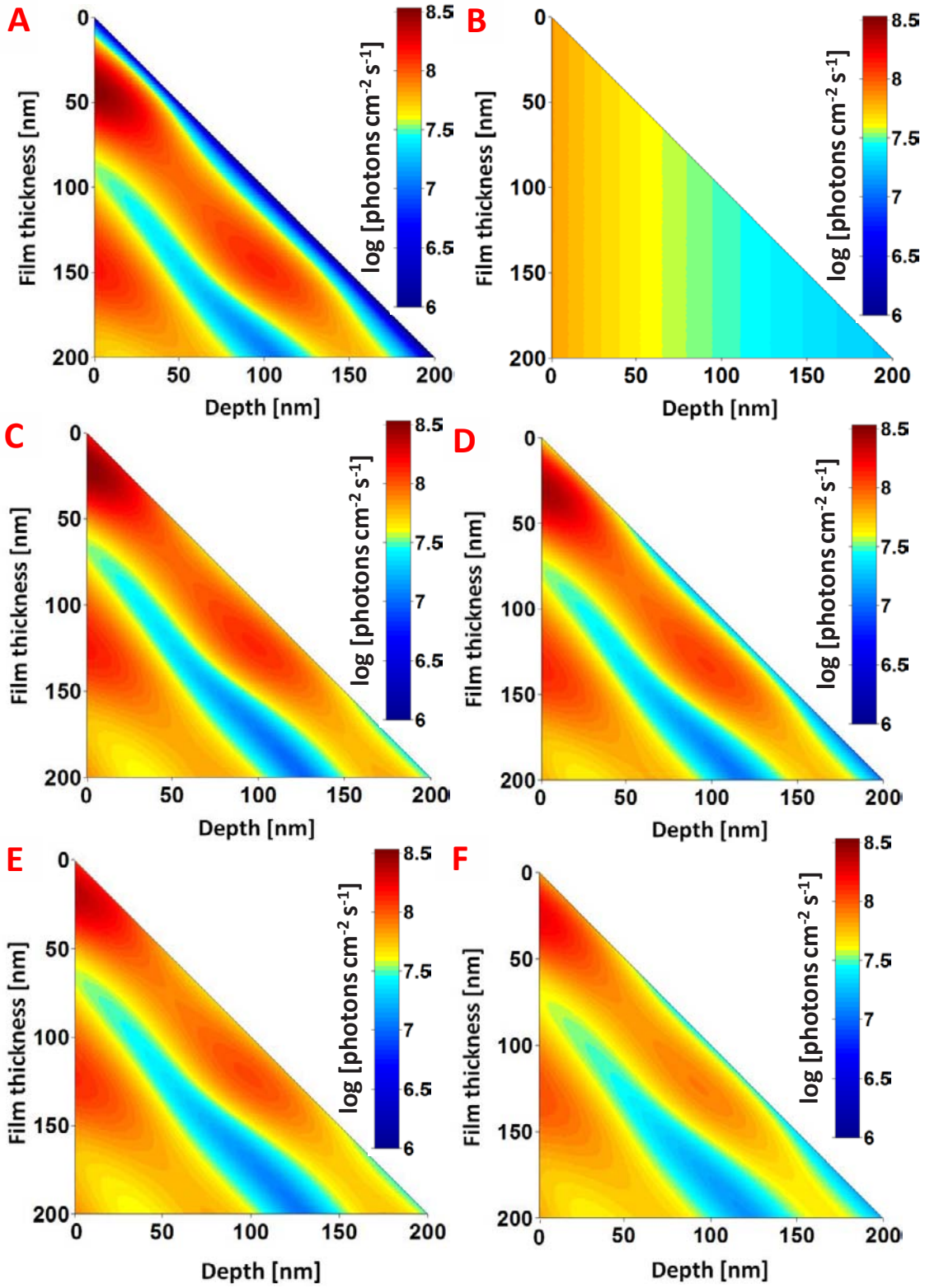

Supplementary Figure S26. Predicted photon flux profiles as a function of film thickness and depth from the surface into the film for Ti-doped α-Fe_2O_3 films on ideally reflective (A), transparent (B), and metalized substrates coated with silver (C), aluminum (D), gold (E) or platinum (F).

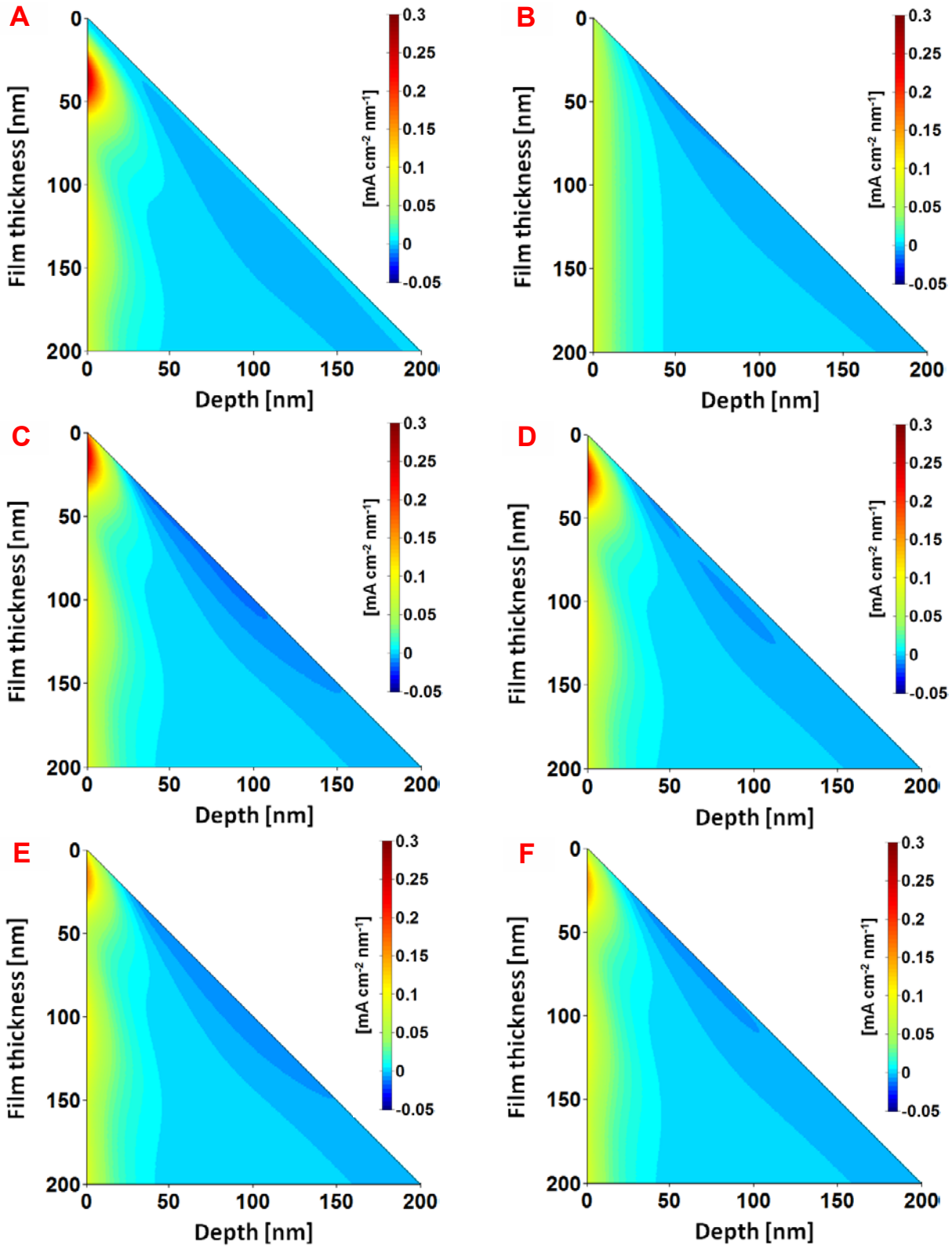

Supplementary Figure S27. The predicted photocurrent density per unit volume profiles as a function of film thickness and depth for Ti-doped α-Fe_2O_3 films on ideally reflective (A), transparent (B), and metalized substrates coated with silver (C), aluminum (D), gold (E) or platinum (F).

DOI: 10.1038/NMAT3477

Supplementary References:

S1. Rottkay, K. V. & Rubin, M. Optical indices of pyrolytic Tin-oxide glass. *Mater. Res. Soc. Symp. Proc.* **426**, 449-455 (1996).

S2. Karlsson, B., Ribbing, C. G., Roos, A., Valkonen, E. & Karlsson, T. Optical properties of some metal oxides in solar absorbers. *Phys. Script* **25**, 826-831 (1982).

S3. Klahr, B. M., Martinson, A. B. F. & Hamann, T. W. Photoelectrochemical Investigation of Ultrathin Film Iron Oxide Solar Cells Prepared by Atomic Layer Deposition. *Langmuir* **27**, 461–468 (2011).

S4. Murphya, A.B., Barnesa, P.R.F., Randeniyaa, L.K., Plumba, I.C., Greyb, I.E., Horneb, M.D. & Glasscock, J.A. Efficiency of solar water splitting using semiconductor electrodes. *Int. J. Hydrogen Energy* **31**, 1999-2017 (2006).

S5. ASTM G173-03, 2008, "Standard Tables for Reference Solar Spectral Irradiances: Direct Normal and Hemispherical on 37° Tilted Surface," ASTM International, West Conshohocken, PA, 2008, DOI: 10.1520/G0173-03R08, http://www.astm.org/Standards/G173.htm.

S6. Lopes, T., Andrade, L., Ribeiro, H. A. & Mendes, A. Characterization of photoelectrochemical cells for water splitting by electrochemical impedance spectroscopy. *Int. J. Hydrogen Energy* **35** 11601-11608 (2010).

S7. Dotan, H., Sivula, K., Grätzel, M., Rothschild, A. & Warren, S. C. Probing the photoelectrochemical properties of Hematite (α-Fe_2O_3) electrodes using Hydrogen Peroxide as a hole scavenger. *Energy Environ. Sci.* **4**, 958-964 (2011).

S8. Tilley, S. D., Cornuz, M., Sivula, K. & Grätzel, M. Light-Induced Water Splitting with Hematite: Improved Nanostructure and Iridium Oxide Catalysis. *Angew. Chem. Int. Ed.* **49**, 6405-6408 (2010).

S9. Kay, A., Cesar, I. & Grätzel, M. New Benchmark for Water Photooxidation by Nanostructured α-Fe_2O_3 Films. *J. Am. Chem. Soc.* **128**, 15714-15721 (2006).